Available online at www.sciencedirect.com
ScienceDirect
Engineering Fracture Mechanics 75 (2008) 4309–4332
Engineering Fracture Mechanics
www.elsevier.com/locate/engfracmech

Cohesive zone simulations of crack growth along a rough interface between two elastic–plastic solids

Pablo D. Zavattieri [a,*], Louis G. Hector Jr. [a], Allan F. Bower [b]

[a] GM Research and Development Center, 30500 Mound Road, Warren, MI 48090, United States
[b] Division of Engineering, Brown University, Providence, RI 02912, United States

Received 7 September 2006; received in revised form 16 October 2007; accepted 7 November 2007
Available online 22 November 2007

Abstract

It has been known for many years that crack propagation along interfaces is influenced by interface topography or roughness profile. This has given rise to a small body of literature in which interface toughening with stochastic surface finishes, produced by grinding, rolling, or grit blasting, has been the primary focus. However, there is very little information currently available on the effect of patterned interfaces that are characterized by a minimal number of geometric parameters. In the present article, roughness-enhanced toughening of a cohesive interface between two identical materials is explored with a pure sinusoidal interface morphology that is characterized by its aspect ratio or ratio of amplitude to wavelength. Sixteen finite element meshes, each with a different aspect ratio, were constructed to study initiation and growth of a semi-infinite interface crack due to remote mode-I loading. The cohesive interface was modeled with a viscosity-modified Xu–Needleman cohesive zone law, and the solids were characterized with continuum elastic and elastic–plastic constitutive models. Predicted relationships between the aspect ratio and the macroscopic toughness point to key differences in the material models. A set of critical parameters which include the aspect ratio, material and cohesive properties is predicted such that catastrophic crack growth is inhibited due to crack blunting. A clear boundary between brittle and ductile fracture behavior is thus identified. The results suggest some guidelines for practical design of failure resistant interfaces through appropriate choice of geometric, material, and cohesive parameters.

Keywords: Cohesive zone model; Sinusoidal interface; Interface fracture; Finite element analysis

1. Introduction

Among the many factors that mitigate the strength of an interface between two materials, it is the morphologies of the bonded surfaces that have yet to be effectively exploited for inhibition of crack propagation (i.e. interfacial toughening). Experiments have suggested that the toughness of an interface between two materials can be enhanced by manipulating surface roughness via etching, hot rolling, grit blasting, or laser ablation

* Corresponding author. Tel.: +1 586 864 2451; fax: +1 586 986 0446.
E-mail address: Pablo.Zavattieri@gm.com (P.D. Zavattieri).

0013-7944/$ - see front matter © 2007 Elsevier Ltd. All rights reserved.
doi:10.1016/j.engfracmech.2007.11.007

[1–5]. The resulting surface finishes, which are essentially stochastic in nature with roughness heights generally distributed in Gaussian profiles (or variations thereof) [6], are thought to provide an extended path length for a growing crack, continually diverting the crack tip as it moves, leading to more efficient energy dissipation. An intriguing approach to addressing these problems is the incorporation of a patterned interface morphology characterized by a small number of (readily quantifiable) geometric features that can be precisely controlled to mitigate crack nucleation and growth. This has been made possible through advances in precision machining processes (e.g. electrical discharge machining) and primary fabrication methods that impart patterned topographies to metal surfaces (e.g. electron beam texturing of steel tools) [7–10].

Patterned surfaces and interfaces are quite common in nature. Among the more familiar examples are sea waves which result from the Kelvin–Helmholtz instability [11]. Similarly, many material systems and materials manufacturing processes either naturally involve patterned interfaces or have incorporated a patterned interface for product and process enhancement. For example, binary mixtures of granular media have recently been found to adopt patterned stripes of segregated grains due to an oscillating shear stress [12]. The interface morphologies of layered composites adopt non-planar geometries with various deformation schemes [13]. The natural wavy tablet microstructure of Mother-of-Pearl nacre has recently been shown to contribute to its strain-hardening properties [14]. Morphological instability in strained SiGe multilayers results in transformation of planar film interfaces to 3D islands or ridge-like morphologies that degrade performance in semiconductor applications [15]. A solid (that is free of hydrostatic strain) in contact with its own vapor or liquid can relieve its elastic energy by producing an undulatory interface [16]. Solidifying materials commonly exhibit interfaces that are non-planar. For example, the well-known Mullins–Sekerka instability in directional solidification results in a cellular dendritic structure at the solid–liquid interface [17]. Variations in carbon content contribute to macro-scale undulation of steel ingot shells often resulting in catastrophic breakout of molten fluid in continuous casting processes [18]. Irregular heat transfer at a moving metal–mold interface in aluminum casting processes also promotes wavy undulations of the order of tens-of-millimeters [19]. A proposed solution to this is the incorporation of a sinusoidal mold surface for control of the solid–liquid interface morphology and solute segregation to an ingot surface [20,21].

Building upon these observations, we model crack propagation along a cohesive interface that follows a pure sinusoidal morphology between identical materials. The key geometric parameter for the interface is its aspect ratio or ratio of amplitude to wavelength (this is in contrast to stochastic surface morphologies that typically require several roughness measures). Unlike previous models of adhesion and crack propagation along undulatory interfaces, we do not restrict the surface aspect ratio such that the amplitude is much smaller than the wavelength [22–26]. Hence, the analysis is carried out within the framework of the finite element method. A viscosity-modified Xu–Needleman traction–displacement law is assumed to govern interfacial decohesion due to crack growth. A set of 16 specially constructed finite element meshes allowed for the study of crack initiation due to remote mode-I loading over a range of aspect ratios. Following a brief overview of model calibration [27], the extent to which the interfacial toughness can be controlled by the sinusoidal aspect ratio is carefully explored for both elastic and elastic-perfectly plastic material models. A set of critical parameters which includes the aspect ratio, material and cohesive properties is predicted such that catastrophic crack growth is inhibited due to crack blunting. A clear boundary between brittle and ductile fracture behavior is thus identified. The results suggest some guidelines that may assist practical design of failure resistant interfaces with patterned microgeometries.

2. Problem formulation

2.1. Model geometry

We assume that two semi-infinite, identical materials are bonded along an interface that follows a sinusoidal morphology with peak-to-valley amplitude $2A$ and wavelength λ. To evaluate the effects of the sinusoidal morphology and associated area extension on the macroscopic fracture toughness of the interface, the growth of a semi-infinite crack along the interface due to remote mode-I loading is considered.

The model geometry is illustrated in Fig. 1. The crack is positioned at one side of the interface and constrained to propagate along the interface when subjected to the remote opening load. A typical finite

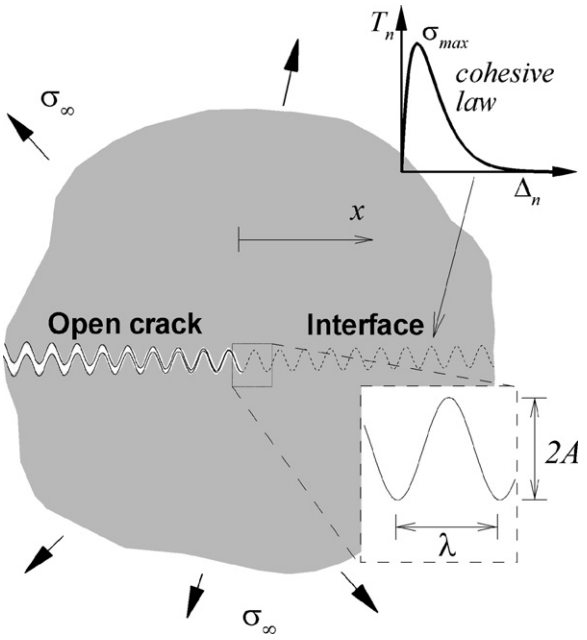

Fig. 1. Schematic of the semi-infinite crack growing along a sinusoidal cohesive interface between two elastic-perfectly plastic solids. The interface is assumed to have a sinusoidal profile with amplitude A and wavelength λ as denoted in the exploded figure.

element mesh is shown in Fig. 2a. The global coordinate system is located at the center of the circular domain as shown in Fig. 2b, with a highly magnified view in Fig. 2c. The sinusoidal interface runs along the x-direction following $y(x) = A[1 + \sin(2\pi\{x - \lambda/4\}/\lambda)]$. The crack tip (also depicted in Fig. 1) is located at the origin of coordinates $(x, y = 0)$. Hence, the interface is "open" for $x < 0$, and connected (or bonded) for $x \geqslant 0$, where zero-thickness cohesive elements are inserted to model interfacial decohesion (see inset to Fig. 2c).

The radius of the model domain in Fig. 2a is R_0, where $R_0 \gg A,\lambda$. This criterion precludes mesh boundary interference on crack propagation along the sinusoid. A close up of the sinusoidal interface near the crack tip is shown in Fig. 2b. The finite element mesh was refined in the crack tip region such that $h/\lambda \approx 10^{-3}$ (where h is the length of the interface elements and, therefore, the edge length of the adjacent quadrilateral finite elements) along the first period where stable crack propagation is expected. After the second period, it is found that $h/\lambda \approx 2 \times 10^{-3}$ to 5×10^{-3}. Due to the non-planar interface and propagating crack, we were unable to take advantage of the apparent symmetry of our model to reduce the size of the computational domain depicted in Fig. 2a. The reader is referred to [27] for a more detailed description of the computational domain and mesh generation.

2.2. Material models

We assume that the uniaxial tensile stress–strain curve for the material has the form

$$\sigma = \begin{cases} E\varepsilon & \text{if } \varepsilon \leqslant \sigma_y/E \\ K\varepsilon^n & \text{if } \varepsilon > \sigma_y/E \end{cases} \tag{1}$$

Note that $K = \sigma_y(E/\sigma_y)^n$, E is Young's Modulus, σ_y is the initial yield stress, n is the strain-hardening exponent, σ is the true effective stress and ε is the logarithmic strain. For the case of an elastic-perfectly plastic material, $n = 0$, and different values of σ_y can be considered since fracture will be flow stress dependent. Yielding is governed by a von Mises isotropic plasticity model.

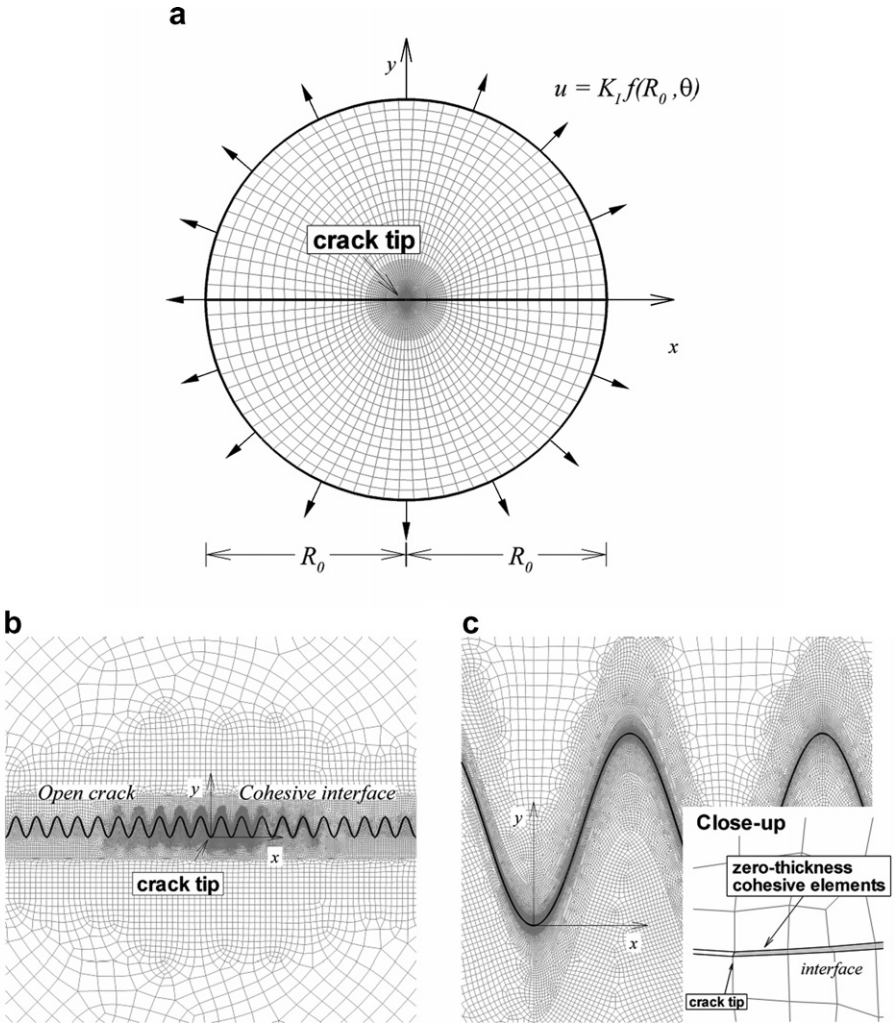

Fig. 2. (a) Sample mesh with $R_0 \gg A$. The sinusoidal interface is at the center of the mesh along the x-axis and hence is not visible. (b) Zoom showing the sinusoidal interface and the crack tip. (c) Region near the crack tip and exploded view showing the cohesive elements.

2.3. Boundary conditions

With the intention of determining the fracture toughness of the model interfaces, load control boundary conditions were applied to induce crack instability [28] and therefore determine the maximum load needed for unstable growth. Only mode-I loading was considered in this work. The boundary conditions consist of displacement fields corresponding to the isotropic elastic mode-I singular field remote from the crack tip (K_I field). According to the classic theory of linear elastic fracture mechanics [28], the displacement components on the remote (circular) boundary (see Fig. 2a) are

$$\begin{aligned} u_x &= \frac{K_I}{\mu}\sqrt{\frac{R_0}{2\pi}}\cos\frac{\theta}{2}\left(1 - 2\nu + \sin^2\frac{\theta}{2}\right) \\ u_y &= \frac{K_I}{\mu}\sqrt{\frac{R_0}{2\pi}}\sin\frac{\theta}{2}\left(2 - 2\nu - \cos^2\frac{\theta}{2}\right) \end{aligned} \tag{2}$$

where $R_0 = \sqrt{x^2 + y^2}$ denotes the outer boundary radius, $\theta = \tan^{-1}(y/x)$, $\mu = E/2(1+\nu)$, ν is Poisson's ratio, with Cartesian coordinates x and y measured relative to the crack tip. The displacement field is only applied to

those nodes located along the outermost circular boundary (as shown in Fig. 2a). Since the boundary conditions are described in terms of the stress intensity factor K_I, the problem does not need to be described by the external applied load and/or the dimensions of the mesh. Therefore, the stress intensity factor K_I will be used to reference the applied load. Since local crack opening is always observed in these calculations (i.e. we allow no crack closure), sliding friction and contact need not be considered.

2.4. Cohesive interface model

During crack growth, a fracture process zone exists ahead of the crack tip. For metals, micro-cracks or micro-voids nucleate, grow, and eventually coalesce with the main crack. Alternatively, crack propagation in fibrous materials occurs by progressive failure of fibers during decohesion. Oxide and grain bridging are additional mechanisms [29]. These micromechanical phenomena are clearly material-dependent and ultimately involve the breaking of bonds which points to the atomistic origins of fracture [30]. We note that the region where the cohesive tractions play an important role in material separation is the cohesive zone.

Crack propagation is effectively modeled by a cohesive traction–separation law (i.e. an interfacial constitutive model). The various material-specific micromechanical mechanisms associated with fracture have led to the development of numerous cohesive zone laws [29] for applications ranging from crazing in glassy polymers [31] to failure in concrete dams and masonry structures [32]. For the sinusoidal interfaces considered herein, we adopt the cohesive traction–separation law proposed by Xu and Needleman [33] that relates the normal and tangential displacement discontinuity across the interface (Δ_n, Δ_t) and the normal and tangential tractions acting on it (T_n, T_t). This relationship is defined by the potential, ϕ, from which the tractions are derived:

$$T_n = \frac{\partial \phi}{\partial \Delta_n}, \quad T_t = \frac{\partial \phi}{\partial \Delta_t} \tag{3}$$

where

$$\phi(\Delta_n, \Delta_t) = \phi_n + \phi_n \exp\left(-\frac{\Delta_n}{\delta_n}\right)\left\{\left[1 - r + \frac{\Delta_n}{\delta_n}\right]\frac{1-q}{r-1} - \left[q + \left(\frac{r-q}{r-1}\right)\frac{\Delta_n}{\delta_n}\right]\exp\left(-\frac{\Delta_t^2}{\delta_t^2}\right)\right\} \tag{4}$$

Note that q and r are parameters that couple the normal and tangential tractions. For simplicity, we choose $q = 1$, and therefore $\phi_t = \phi_n$ (unless otherwise indicated). Preliminary studies suggest no effect on the parameter r because of the absence of compression along the interface [34]. Therefore, for simplicity we choose, $r = 0$.

Following Gao and Bower [35], we use a mechanism for dissipating the excess energy to improve the likelihood that the numerical procedure will converge for a sufficiently small time-step. This involves the addition of an artificial viscosity to the traction–displacement law (for $q = 1$, $r = 0$). Inserting Eq. (4) into Eq. (3), and adding the artificial viscosity gives the following traction–displacement relationships:

$$\begin{aligned} T_n(\Delta_n, \Delta_t) &= \sigma_{\max}\frac{\Delta_n}{\delta_n}\exp\left(1 - \frac{\Delta_n}{\delta_n} - \frac{\Delta_t^2}{\delta_t^2}\right) + \xi_n \frac{\mathrm{d}}{\mathrm{d}t}\left(\frac{\Delta_n}{\delta_n}\right) \\ T_t(\Delta_n, \Delta_t) &= 2\sigma_{\max}\left(\frac{\delta_n}{\delta_t}\right)\frac{\Delta_t}{\delta_t}\left(1 + \frac{\Delta_n}{\delta_n}\right)\exp\left(1 - \frac{\Delta_n}{\delta_n} - \frac{\Delta_t^2}{\delta_t^2}\right) + \xi_t \frac{\mathrm{d}}{\mathrm{d}t}\left(\frac{\Delta_t}{\delta_t}\right) \end{aligned} \tag{5}$$

where ξ_n and ξ_t are (adjustable) viscosity parameters that govern viscous energy dissipation at the interface due to normal and tangential loading, respectively. The viscosity does not model any macroscopic-scale energy dissipation process. Rather, it is introduced to regularize instabilities that tend to occur when a crack first initiates at the weak interface. In this work, both viscosity parameters are chosen to be identical. Under normal loading, the interface has a work of separation, ϕ_n, and the normal traction reaches a maximum value $\sigma_{\max} = \phi_n/(\delta_n e)$ at an interfacial separation $\Delta_n = \delta_n$. We will refer to $\sigma_{\max}$ as the intrinsic cohesive strength of the interface. Under pure shear loading, the interface has work of separation ϕ_t where $\phi_t = q\phi_n$, and the tangential traction reaches a maximum value at $\Delta_t = \delta_t/\sqrt{2}$. Therefore, the quantities δ_n and δ_t are called the critical opening and tangential displacements. The normal work of separation is, therefore, defined as

$\phi_n = \int_0^\infty T_n \mathrm{d}\Delta_n = \sigma_{\max}\delta_n e$. Although we constrain crack propagation to follow the sinusoidal interface (see Fig. 1), in practice some material systems (e.g. aluminum bonded to diamond [30]) will likely fail outside of the interface due to crack propagation into the weaker of the two materials. Such a situation, although beyond the scope of the present work, can readily be modeled by inserting cohesive nodes not only along the interface but also in regions of both materials that surround the interface.

2.5. Finite element procedure

The commercial finite element code ABAQUS/Standard [36] was used for all simulations. All models assumed a 2D plane strain condition. Elements in the solid materials were represented by 4-node quadrilateral continuum elements. The weak sinusoidal interface was represented by 4-node, zero-thickness interface elements in which the cohesive traction–displacement law is accounted for in a user-defined subroutine (UEL). The description of the weak interface assumes that these "cohesive" interface elements carry forces that oppose normal separation and shear between the two surfaces following Eq. (5). The degradation of the traction in the cohesive zone can be interpreted as progressive decohesion or failure of the interface until the traction is zero. Beyond that point, the two surfaces will behave as distinct entities. Crack propagation can therefore be simulated as the consecutive failure of these cohesive elements. Since the most important information from this analysis can be obtained from crack propagation along the first period, cohesive interface elements were only embedded along the first three periods of each sinusoid.

2.6. Macroscopic interface fracture toughness and dimensional analysis

Of particular interest here is determination of a quantitative relationship between the macroscopic or critical interface toughness, K_{Ic}, which corresponds to unstable crack tip growth or growth without an increase in the applied load, and key material properties and geometric parameters. This requires a suitable dimensional analysis to determine those parameters that are likely to have the most effect on K_{Ic}. We first plot the crack tip position (x, y) as a function of the applied load K_{I} and determine the regime of unstable crack propagation. The crack tip position is defined at the point where $\sqrt{(\delta_n/\Delta_n)^2 + (\delta_t/\Delta_t)^2} \geqslant 5$ is satisfied, which means that $T_n/\sigma_{\max} < 0.1$. Fig. 3 shows the evolution of the x-coordinate of the crack tip position as a function of the

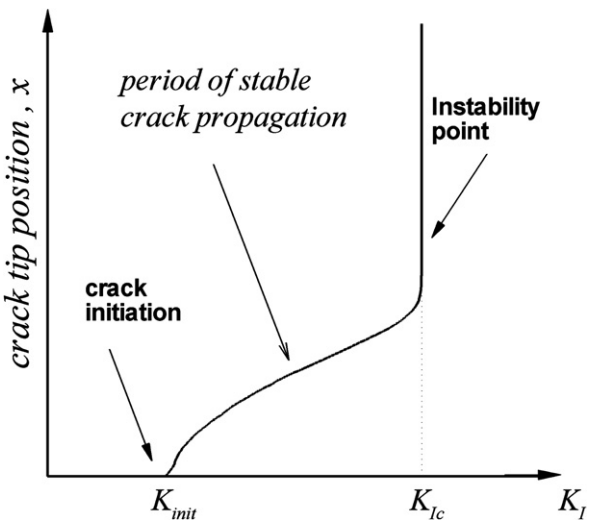

Fig. 3. x-coordinate of the crack tip as K_{I} is increased. K_{init} is the point where the crack starts to propagate. The instability point is indicated where the crack grows catastrophically. That is the point where we extract the critical value of $K_{\mathrm{I}} = K_{\mathrm{Ic}}$ as the macroscopic fracture toughness.

applied load, K_I. The first part of the curve is associated with crack initiation followed by stable crack propagation, as indicated in the figure. The point of intersection between the curved and vertical parts of the curve (i.e. $K_{Ic} = K_I$ or the macroscopic toughness) denotes the onset of unstable crack growth. To confirm this behavior, similar calculations were repeated in which the load was ramped up to different values of K_I/K_0 and subsequently held fixed to determine if either stable or unstable crack growth resulted without any increase in the applied load. We confirmed that the true instability point is given by K_{Ic}/K_0.

In order to establish a framework for a dimensional analysis, the main dimensional groups must be identified. The geometrical parameters describing the shape of the sinusoidal interface are the peak-to-valley amplitude, $2A$, and wavelength, λ. The material parameters are Young's Modulus, E, Poisson's ratio, v, yield stress, σ_y, and the hardening exponent, n (see Eq. (1)). Finally, the cohesive interface parameters specified by the traction–displacement law (see Eq. (5)) are σ_{max}, δ_n, δ_t, r and q. As discussed in [27], the effects of varying the coupling parameters are negligible for the range of aspect ratios considered herein, and we therefore chose $q = 1$(or $\phi_n = \phi_t$), $r = 0$ and $\delta_n = \delta_t$.

The macroscopic or critical fracture toughness, K_{Ic}, can be written in the following functional form:

$$K_{Ic} = f(A, \lambda, E, v, \sigma_y, n, \sigma_{max}, \delta_n) \tag{6}$$

The next step is to find the relevant combinations of physical variables in dimensional groups, Π_i, following Buckingham's 'Π-theorem' [37], such that Eq. (6) can be written as $\Pi_0 = \Gamma(\Pi_1, \Pi_2, \Pi_3, \Pi_4, \Pi_5)$. The choice of appropriate Π_i requires an understanding of both the physical processes and the relevant material properties and geometric variables. In our analysis, we initially chose the following dimensionless variables: $\Pi_0 = K_{Ic}/(E\sigma_{max}\delta_n)^{1/2}$, $\Pi_1 = E/\sigma_{max}$, $\Pi_2 = \sigma_y/\sigma_{max}$, $\Pi_3 = \delta_n/\lambda$, $\Pi_4 = A/\lambda$, $\Pi_5 = n$ and $\Pi_6 = v$. However, it is possible to make use of some other concepts to express these variables in a more succinct fashion, making it easier to interpret the results. According to the Griffith criterion [28], the work of separation, $\phi_n = \sigma_{max}\delta_n e$, is the critical energy release rate due to fracture, and can be used to express the intrinsic (or local) fracture toughness of the interface, K_0, as follows:

$$K_0 = \sqrt{\frac{E\phi_n}{(1-v^2)}} \tag{7}$$

Therefore, Π_0 can be rewritten as $\Pi_0' = K_{Ic}/K_0$. This allows for comparison of the interface fracture toughness with the intrinsic fracture toughness of a planar interface in the absence of plasticity. Π_1 and Π_2 were chosen such that the intrinsic cohesive strength could be compared with the Young's modulus and the yield stress of the material. In particular, we expect Π_2 to be of importance since it will allow us to evaluate the competition between plastic deformation and interfacial fracture. On the other hand, Π_3 can be combined with Π_1 and rewritten as $\Pi_3' = l_{cz}/\lambda$, where l_{cz} is the cohesive zone length, defined as $l_{cz} = 9\pi(K_0/\sigma_{max})^2/32$ [38]. The cohesive zone length is the length over which the various micromechanical mechanisms associated with fracture (detailed briefly above) are active (a more thorough overview of these mechanisms can be found in [29]). A second possibility is to combine Π_3' with Π_2 and obtain $\Pi_3'' = \Gamma_p/\lambda$, where Γ_p is yet another characteristic length that describes the plane-strain plastic zone size in a von Mises solid. This is defined as $\Gamma_p = (K_0/\sigma_y)^2/3\pi$ [39]. Depending upon how the results are presented it is possible to opt for one or another. Another relationship between the two characteristic lengths is given by $l_{cz}/\Gamma_p = 27\pi^2\Pi_2^2/32$. Using these dimensionless variables, Eq. (6) can be rewritten as a normalized macroscopic fracture toughness as follows:

$$\frac{K_{Ic}}{K_0} = \Gamma\left(\frac{\sigma_y}{\sigma_{max}}, \frac{E}{\sigma_{max}}, v, n, \frac{l_{cz}}{\lambda}, \frac{A}{\lambda}\right) \tag{8}$$

The finite element simulations of the different sinusoidal interfaces are then used to determine the extent to which the normalized fracture toughness, K_{Ic}/K_0, depends upon each dimensionless group. It would be desirable to write an explicit functional form of Eq. (8). We anticipate that this is be possible since Eq. (8) is likely to depend upon more than one parameter and hence represents a multi-dimensional surface in parameter space. However, we can interrogate this surface numerically by exploring suitable projections involving relationships between two sets of parameters. This allows us to better understand how these relationships could conceivably be used for interface design in response to the applied mode-I loading.

2.7. Additional numerical aspects

The model parameters in Eq. (8) govern the macroscopic behavior of the sinusoidal interface. However, there is a group of variables, introduced to facilitate the numerical methodology, which must be established prior to running the crack propagation simulations. These are: the element size, h, the model domain radius, R_0, the viscosity, ξ, and the load increment, ΔK_I. In [27], detailed convergence tests were conducted to establish appropriate values for these parameters to ensure that they do not artificially affect the results. The major results from [27] are incorporated herein without further elaboration.

In addition to an element size with $h/\lambda \approx 10^{-3}$ along the first period of the sinusoid (necessary for good definition of the stress concentration near the crack tip), other characteristic lengths play an important role in the simulations [27]. For example,

$$h \ll l_{cz} \ll \max(\lambda, A) \ll R_0 \tag{9}$$

Since h/λ is fixed, the cohesive parameters from Eq. (5) have been chosen such that Eq. (9) is satisfied. A convergence analysis directed us to meshes with $R_0 = 5 \times 10^3 \lambda$.

The viscous term, ξ, in Eq. (5) becomes important when the displacement rates increase, especially when unstable equilibrium is achieved at the onset of catastrophic crack propagation. A slight damping of the crack growth gives place to a slower growth when the instability is triggered. Although the crack speed obtained with this method is inaccurate, the critical load at which the crack becomes unstable is well defined, and therefore leads to a more physically meaningful prediction of the interface fracture toughness, K_{Ic}. Reasonable values of ξ should be small enough to preclude excessive artificial viscosity, but not so small as to create numerical instabilities that force termination of the calculation before crack instability. After thorough scrutiny, it was found that a value of $\Xi = \xi \dot{K}_I/(\sigma_{max} K_0) \approx 1 \times 10^{-5}$ (where Ξ is the dimensionless viscosity) was deemed small enough to obtain an acceptable error margin (see [27] for additional details). Finally, a loading step of $\Delta K_I/K_0 \approx 0.003$ was adopted for all calculations.

3. Interface toughness prediction for elastic materials

For elastic materials, the sinusoidal aspect ratio was the only parameter that had an impact on the normalized macroscopic fracture toughness (corresponding to unstable crack growth). The relationship $K_{Ic}/K_0 = \Gamma(A/\lambda)$ is essentially linear at larger values of A/λ (i.e. $A/\lambda > 0.25$) and the following functional form is appropriate:

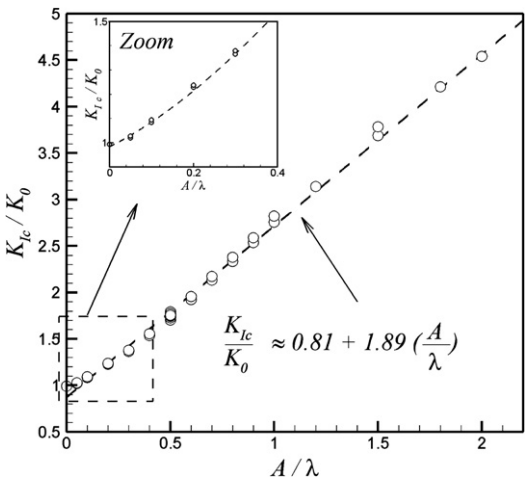

Fig. 4. Macroscopic interface fracture toughness as a function of the aspect ratio for an interface between two identical elastic solids.

$$\frac{K_{Ic}}{K_0} \approx 0.81 + 1.89\left(\frac{A}{\lambda}\right) \tag{10}$$

Fig. 4 shows the macroscopic, K_{Ic}/K_0, as a function of A/λ. This linear relationship has been confirmed by further numerical studies using the J-integral in [27]. The inset figure shows the variation of K_{Ic}/K_0 for the smallest values of A/λ. This relationship shows a clear tendency to the Griffith criterion $K_{Ic} \to K_0$ when $A/\lambda \to 0$ and suggests that for fixed wavelength, increasing the peak-to-valley heights of the sinusoidal asperities effectively delays unstable crack growth. It should be noted that the ability to acquire robust numerical results for small aspect ratios progressively worsens as $A/\lambda \to 0$, a feature that results from the difficulties associated with identifying the crack instability point as it gets closer to the crack initiation point. We surmise that existing analytical solutions may be more appropriate to capture the right crack behavior for $0 < \frac{A}{\lambda} \leqslant 0.25$ and may in fact be used as starting solutions for the finite element simulations within this range of aspect ratios [22–26]. Moreover, the authors have recently shown that $K_{Ic}/K_0 = 2/(1 + [1 + 4\pi^2(A/\lambda)^2]^{-1/2})$ for $A/\lambda \leqslant 0.25$ using arguments borrowed from linear elastic fracture mechanics [27].

4. Interface toughness prediction for elastic-perfectly plastic materials

It is well established that plastic deformation in metals has a large impact on fracture toughness. With plasticity, the external work needed to propagate a crack is much larger than the energy required for material separation. Tvergaard and Hutchinson [40,41] developed one of the first models to use a cohesive zone law for cleavage fracture by atomic separation and a continuum model to represent the plastic deformation. They considered a straight crack in an infinite solid and their analysis consisted on finding the critical dimensional groups that influenced the toughness for initiation and steady-state crack propagation. The combination of a traction–displacement law with an isotropic plasticity model allowed prediction of many aspects of the fracture behavior of metals. In the present work, we use similar tools to investigate crack behavior in a plastic material containing an interface with a non-planar (i.e. sinusoidal) geometry.

In this section, we first explore the conditions for ductile to brittle transition in an elastic-perfectly plastic material as predicted by the variation of the normalized flow stress with normalized toughness. A single sinusoidal aspect ratio is chosen for this purpose. We then explore the influence of the elastic parameters E and ν on the macroscopic fracture toughness. The characteristic lengths δ_n/λ, l_{cz}/λ and the ratio l_{cz}/Γ_p are investigated since these affect K_{Ic}/K_0. Finally, a relationship between K_{Ic}/K_0 for an elastic-perfectly plastic material and the sinusoid aspect ratio is developed.

4.1. Transition from brittle to ductile fracture: effect of the normalized yield stress, σ_y/σ_{max} for fixed A/λ

We examine the effects of the cohesive interface and material parameters on the normalized interface fracture toughness K_{Ic}/K_0 of an interface with $A/\lambda = 0.5$. The influence of the individual material-related dimensionless variables will be independently evaluated in a subsequent section.

We begin by testing the effect of σ_y/σ_{max} in an elastic-perfectly plastic material ($n = 0$) for $E/\sigma_{max} = 100$, $\nu = 0.3$ and $l_{cz}/\lambda = 1/4$. Fig. 5 shows the evolution of the normalized x-coordinate of the crack tip position, x/λ, as a function of the applied load, K_I/K_0 for several values of σ_y/σ_{max}. Two distinct behaviors are evident in Fig. 5. One behavior, resembling that depicted in Fig. 3, is unstable crack growth at a point in the first half of the first sinusoidal period (i.e. $x/\lambda < 0.5$). The second behavior is associated with very slow and stable crack growth as suggested by the curves that increase gradually with K_I/K_0. In the first behavior, the crack evolution asymptotically approaches the elastic solution as σ_y/σ_{max} increases (to the limit where $\sigma_y/\sigma_{max} \to \infty$). This behavior is shown by the curves that turn vertically upwards. In fact, a value of $\sigma_y/\sigma_{max} \geqslant 2$ is high enough to obtain a fracture toughness K_{Ic}/K_0 similar to that obtained with an elastic solid. The elastic solution (denoted by the solid black line closest to the ordinate axis) was also included in Fig. 5 for comparison. Note that as σ_y/σ_{max} decreases, the instability point is delayed to higher loads (in other words, the macroscopic interface toughness K_{Ic}/K_0 increases). This behavior is observed until a critical value of the normalized yield stress is reached where the crack simply keeps growing without becoming unstable. This critical value marks a

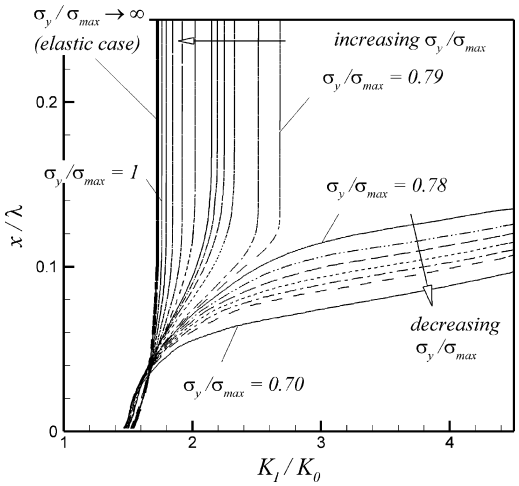

Fig. 5. Normalized crack tip position (projected over the x-axis) as K_I is increased for different values of σ_y/σ_{max} for $A/\lambda = 0.5$, $E/\sigma_{max} = 100$ and $l_{cz}/\lambda = 2.64$ and $n = 0$. Crack instability only occurs for $\sigma_y/\sigma_{max} \geqslant 0.79$. For $\sigma_y/\sigma_{max} < 0.78$, the crack propagates in a stable manner.

well defined transition to the second behavior. This "jump" to the second set of more gradually increasing curves in Fig. 5 occurs at approximately $(\sigma_y/\sigma_{max})_{cr} = 0.785 \pm 0.05$ (for this particular set of parameters). In other words, continuous, stable crack propagation behavior occurs for $\sigma_y/\sigma_{max} \leqslant 0.78$. In this range, the crack evolution curves are similar to those in previous models of straight crack growth [40,41] where the resistance to fracture increases monotonically without any transition to unstable crack propagation. A closer examination around the crack tip reveals that the transition to stable crack growth is due to the competition between the ability of the material to dissipate energy via plastic deformation with the ability of the interface to open up. Stable crack growth results when the interface effectively dissipates accumulated energy into plastic deformation instead of rapid and uncontrolled interfacial decohesion. Fig. 5 clearly demonstrates the transition from unstable to stable crack growth due to both the plasticity material model and the non-planar interface. Fig. 6a and b shows the effective plastic strain, ε^p_{eff}, as the crack progresses (for a load of $K_I/K_0 \approx 2.2$) for $\sigma_y/\sigma_{max} = 0.79$ and $\sigma_y/\sigma_{max} = 0.78$, respectively. Note that these values are very close to the critical value $(\sigma_y/\sigma_{max})_{cr}$. The extent of plastic deformation is clearly greater in Fig. 6b as expected, with significant plastic strain accumulating at distances well removed from the interface. Fig. 6c and d shows magnified views of the deformed mesh near the crack tip for both cases. While the case with higher yield stress shows a sharp crack tip, the case with $\sigma_y/\sigma_{max} = 0.78$ shows a more rounded crack tip confirming the tendency of material surrounding the crack to plastically deform and hence blunt (or arrest) crack growth: this behavior could not be observed with the elastic material model [27]. This makes crack growth more stable by requiring higher loads to propagate the crack tip thereby resulting in behavior that is captured in the resistance curves of Fig. 5 for $\sigma_y/\sigma_{max} < (\sigma_y/\sigma_{max})_{cr}$.

Determination of the critical value of the normalized yield stress $(\sigma_y/\sigma_{max})_{cr}$ relies upon two key issues:

(1) The crack tip shape must be very well defined. It is sharp for $\sigma_y/\sigma_{max} > (\sigma_y/\sigma_{max})_{cr}$ and blunted for $\sigma_y/\sigma_{max} < (\sigma_y/\sigma_{max})_{cr}$. The transition from one regime to the other (i.e. unstable growth to blunting) is characterized by a "jump" over a very narrow range of (σ_y/σ_{max}) (the calculations can be refined even more to define the narrow range of $(\sigma_y/\sigma_{max})_{cr}$ over which this transition takes place).
(2) The required load to propagate the crack increases significantly for $\sigma_y/\sigma_{max} < (\sigma_y/\sigma_{max})_{cr}$, and no instability is observed in the calculations. The simulations suggest that there is a significant amount of plastic deformation together with highly distorted elements even when the crack tip position is $x/\lambda < 0.2$. These conditions forced the calculation to stop (see Fig. 6d). It may be possible that adaptive meshing [42] or calculation with mesh-free methods [43] will overcome this difficulty thereby allowing the simulation of crack growth beyond this point (and perhaps to a condition of steady-state growth) [40].

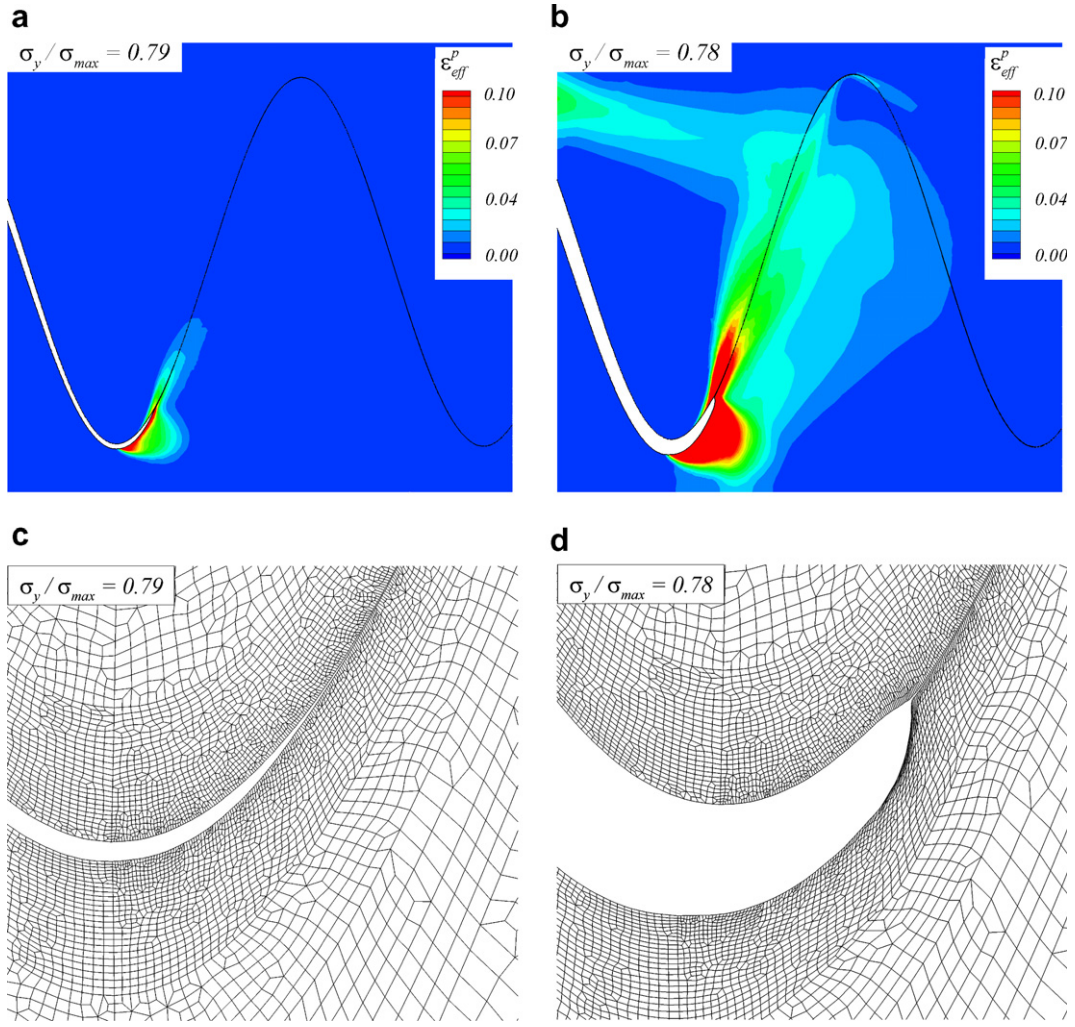

Fig. 6. Detailed views of the crack tip for transition from brittle behavior to stable crack growth with blunting for $A/\lambda = 0.5$. (a) Effective plastic strain field for $\sigma_y/\sigma_{max} = 0.79$. (b) Effective plastic strain field for $\sigma_y/\sigma_{max} = 0.78$. (c and d) Close-up views of the deformed meshes that show the differences in deformation around the crack tip. Blunting is evident in (d).

The crack evolution shown in Fig. 3 suggests that two important parameters can be extracted, namely, the critical load to initiate crack growth, K_{init}/K_0, and the load to induce unstable crack growth (or macroscopic interface toughness) K_{Ic}/K_0. Both parameters provide important insight into the various regimes of fracture behavior as a function of σ_y/σ_{max}. Fig. 7 further explores this by showing $K_{init}/K_0 = f(\sigma_y/\sigma_{max})$ and $K_{Ic}/K_0 = f(\sigma_y/\sigma_{max})$ obtained from the curves in Fig. 5. The dashed line with white diamonds (curve closest to the abscissa) denotes the points where the crack starts growing for a specific σ_y/σ_{max}. The solid line with black circles and white triangles denotes the conditions for unstable crack growth. The white triangles in the instability curve indicate those cases where different combinations of material and cohesive parameters have been chosen in order to have the same $E/\sigma_{max} = 100$ and $l_{cz}/\lambda = 1/4$ (for example $E = 70$ GPa/$\sigma_{max} = 0.7$ GPa should give the same results as $E = 200$ GPa/$\sigma_{max} = 2.0$ GPa). This confirms the validity of using E/σ_{max} as a dimensionless group in Eq. (8). The curve $K_{Ic}/K_0 = f(\sigma_y/\sigma_{max})$ (solid line) has two distinct asymptotes. The horizontal asymptote corresponds to the elastic limit for $\sigma_y/\sigma_{max} \to \infty$, for which $K_{Ic}/K_0 \to 1.73$ (for $A/\lambda = 0.5$). The vertical asymptote for $\sigma_y/\sigma_{max} \to (\sigma_y/\sigma_{max})_{cr}$ where $K_{Ic}/K_0 \to \infty$, indicates the onset of crack blunting.

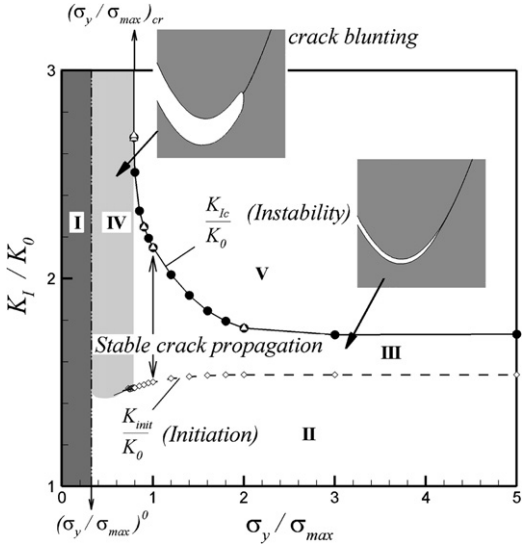

Fig. 7. This plot of the crack initiation point (K_{init}/K_0) and instability (K_{Ic}/K_0) as a function of σ_y/σ_{max} serves as a map of the different crack propagation regimes (identified by roman numerals): I and II are the regions where there is no crack propagation. Regions III and IV denote the regime of stable crack propagation. Region IV is a regime of stable crack propagation with large plastic dissipation where crack blunting occurs. The transition from regimen III to IV occurs at $\sigma_y/\sigma_{max} = 0.78$. Region V is the regime of unstable crack propagation. This particular set of calculation is for an aspect ratio of $A/\lambda = 0.5$.

Fig. 7 depicts regimes (identified by roman numerals) of characteristic crack behaviors:

- Regimes I and II denote no crack propagation. In particular, regime I denotes those cases where the stress acting on the plane ahead of the crack tip never reaches the required peak traction to open the cohesive interface irrespective of the applied external load, and hence $\sigma_y/\sigma_{max} < (\sigma_y/\sigma_{max})^0$. Note that $(\sigma_y/\sigma_{max})^0$ is the threshold value of the normalized yield stress, at which the crack cannot propagate in an elastic-perfectly plastic solid. $(\sigma_y/\sigma_{max})^0$ is indicated in Fig. 7 as a vertical line between regimes I and IV. The model for an elastic-perfectly plastic material predicts that the opening stress lies in the range $0 < \sigma < \sigma_{max}$. Regime II is associated with the case where the applied load is too low to initiate crack propagation ($K_I < K_{init}$).
- Regimes III and IV denote the stable crack propagation regime. In regime III, crack propagation is stable but without a fully developed plastic zone (Fig. 6a and c). Region IV denotes stable crack propagation with large plastic dissipation and crack blunting (see Fig. 6b and d). As previously discussed, the transition from III to IV occurs at $(\sigma_y/\sigma_{max})_{cr}$ (in this particular case $(\sigma_y/\sigma_{max})_{cr} \approx 0.785$).
- Regime V denotes the unstable crack propagation regime for $\sigma_y/\sigma_{max} \geqslant (\sigma_y/\sigma_{max})_{cr}$ and $K_I/K_0 \geqslant K_{Ic}/K_0$.

Hence, three distinctive types of crack evolution for a given material/interface system exit when the load is ramped up from $K_{Ic}/K_0 = 0$:

Type 1 For $\sigma_y/\sigma_{max} \geqslant (\sigma_y/\sigma_{max})_{cr}$, crack growth follows regimes II → III → V. Hence, the crack initially does not grow for $K_{Ic}/K_0 < K_{init}/K_0$ (regime II). Stable growth then occurs according to $K_{init}/K_0 \leqslant K_{Ic}/K_0 < K_{Ic}/K_0$ with minimal plastic deformation and no crack blunting (regime III) until it becomes unstable for $K_{Ic}/K_0 \geqslant K_{Ic}/K_0$. We refer to this as brittle behavior without a fully developed plastic zone (small-scale yielding).

Type 2 For $(\sigma_y/\sigma_{max})^0 < \sigma_y/\sigma_{max} < (\sigma_y/\sigma_{max})_{cr}$, the crack growth behavior passes through regimes II → IV. Following initiation at $K_{Ic}/K_0 > K_{init}/K_0$, the crack grows in a stable manner and later blunts, requiring even higher loads to advance. This is ductile crack propagation.

Type 3 For $\sigma_y/\sigma_{max} < (\sigma_y/\sigma_{max})^0$, crack growth never initiates. Extremely large plastic deformation can develop at the crack tip region inducing blunting without decohesion (regime I). This type of crack evolution only occurs in elastic-perfectly plastic materials.

Calculations with lower values of σ_y/σ_{max} were also conducted. For $\sigma_y/\sigma_{max} < 0.35$, the crack growth does not initiate, indicating the onset of regime I. In fact, this is consistent with the calculations reported in [40] for a straight crack (i.e. along a planar interface), and the fact that the normal traction acting on the plane ahead of the crack tip cannot exceed $\sigma_{yy} = 2.97\sigma_y$ in an elastic-perfectly plastic solid [44]. However, the reliability of the results for $\sigma_y/\sigma_{max} < 0.5$ is compromised to a certain extent due to the development of highly distorted elements near the crack tip region. This results in non-convergence due to the ill-conditioned set of equations that must be solved by ABAQUS. Note that the lower curve K_{init}/K_0 vs. σ_y/σ_{max} could not be defined for $\sigma_y/\sigma_{max} < 0.5$ due to mesh distortion. Nevertheless, determination of $(\sigma_y/\sigma_{max})^0$ is not the main purpose of the current effort since primary focus is on the analysis of the upper curve of Fig. 7, K_{Ic}/K_0 as a function of the variables in Eq. (8).

Figs. 5–7 suggest that the onset of crack instability, which we define as the macroscopic interface toughness K_{Ic}/K_0, is greatly affected by the normalized yield stress σ_y/σ_{max} to the point where there exists a critical value $(\sigma_y/\sigma_{max})_{cr}$ at which the fracture transitions from brittle to a ductile. This is a very important observation in terms of our original objectives because Eq. (8) does not take into account the existence $(\sigma_y/\sigma_{max})_{cr}$ at which there is a well-defined transition in crack behavior. This may be an important design variable that can lead to a tougher interface by modifying the right material and geometrical parameters. As mentioned before, $(\sigma_y/\sigma_{max})_{cr} = 0.785$ for an elastic-perfectly plastic material ($n = 0$), $E/\sigma_{max} = 100$, $\nu = 0.3$ and $l_{cz}/\lambda = 1/4$. How these variables affect $(\sigma_y/\sigma_{max})_{cr}$ requires separate investigation and for this purpose, we introduce a second equation (similar to Eq. (8)) in which $(\sigma_y/\sigma_{max})_{cr}$ is written as a function of the remaining dimensionless groups defined in Section 2.6:

$$\left(\frac{\sigma_y}{\sigma_{max}}\right)_{cr} = \Psi\left(\frac{E}{\sigma_{max}}, \nu, n, \frac{l_{cz}}{\lambda}, \frac{A}{\lambda}\right) \tag{11}$$

We evaluate this equation in the subsequent sections to understand the role of each individual variable.

On the other hand, we observed that the stable crack propagation regime (regime III in Fig. 7) is primarily controlled by the interface geometry. In fact, this behavior is not present for $A/\lambda \to 0$ (the straight crack limit) under quasi-static equilibrium. Many of the material/interface systems of interest will exhibit behavior that falls into Type 1 of crack evolution (for high values of σ_y/σ_{max}), and stable crack propagation can be promoted by increasing the macroscopic fracture toughness (either by delaying the onset of unstable crack propagation or by decreasing σ_y/σ_{max}).

4.2. Influence of the elastic parameters E and ν on crack behavior

The effect of the elastic parameters E and ν on the crack behavior are evaluated for $l_{cz}/\lambda = 1/4$ and $n = 0$, for $A/\lambda = 0.5$. Fig. 8a shows the influence of E/σ_{max} on the macroscopic fracture toughness K_{Ic}/K_0 for two values of σ_y/σ_{max} (0.9 and 1.8). For the range of E/σ_{max} considered, we keep $\nu = 0.3$. The same figure includes the effect of ν when $E/\sigma_{max} = 100$ and $\sigma_y/\sigma_{max} = 1.0$. The crack evolution (normalized crack tip position as a function of the applied load K_I/K_0) is shown in the inset figure at the upper-right corner for $\sigma_y/\sigma_{max} = 0.9$. Clearly, crack growth initiation is not significantly affected by E, whereas the instability point is more sensitive at lower values of E/σ_{max}. The main plot also suggests that the macroscopic interface toughness K_{Ic}/K_0 remains almost constant over the range of E/σ_{max} considered, except for a slight increase at lower values E/σ_{max}. The material is more compliant for $E/\sigma_{max} < 50$, thereby allowing more deformation near the crack tip and unstable crack propagation is consequently delayed. The change in K_{Ic}/K_0 is more pronounced for lower values of σ_y/σ_{max}. There is a clear benefit of lowering the values of E/σ_{max} and σ_y/σ_{max} since doing so leads to larger values of K_{Ic}/K_0. Hence, fixing the material parameters provides an opportunity for some improvement in K_{Ic}/K_0 (i.e. an increase) by directly increasing the intrinsic cohesive strength σ_{max}. However, lowering E/σ_{max} (for example for σ_y/σ_{max}=0.9) does not improve K_{Ic}/K_0 by more than approximately 15% (see the solid line with empty circles in Fig. 8a).

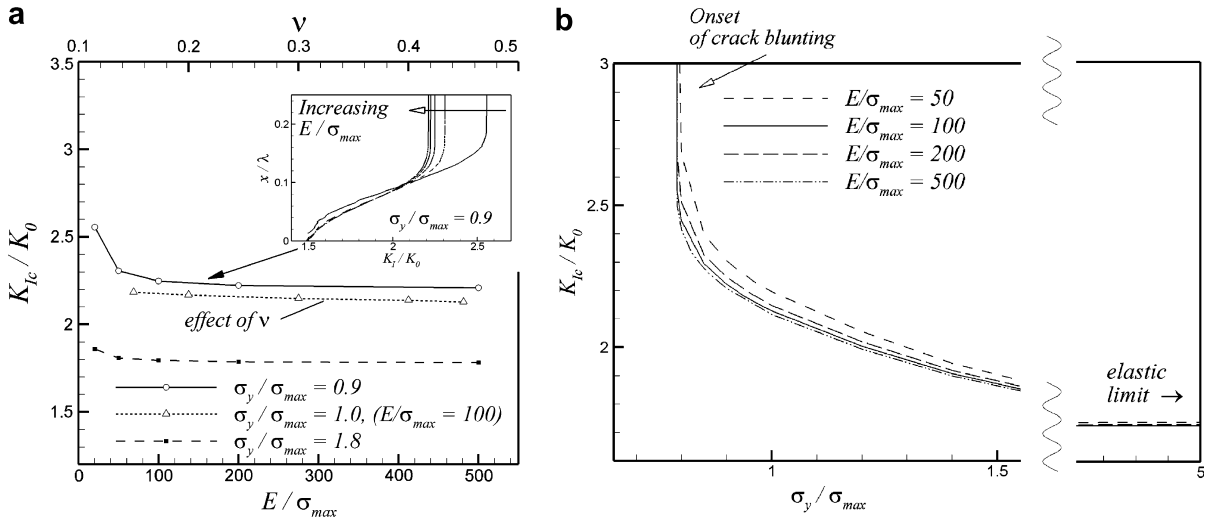

Fig. 8. (a) Effect of E/σ_{max} for two values of $\sigma_y/\sigma_{max} = 0.9$ and 1.8. The enclosed figure in the upper-right corner shows an example of the effect of the normalized Young's Modulus on the crack evolution. The effect of Poisson's ratio, v, is also included in the same figure for comparison purposes for $\sigma_y/\sigma_{max} = 1.0$ and $E/\sigma_{max} = 100$. (b) Effect of E/σ_{max} on the K_{Ic}/K_0 vs. σ_y/σ_{max} curve clearly shows that there is slight shift in K_{Ic}/K_0 for different elastic modulus. However, the critical yield stress $(\sigma_y/\sigma_{max})_{cr}$ remains unaffected. The calculation presented in this figure corresponds to an aspect ratio of $A/\lambda = 0.5$.

For comparison, the influence of Poisson's ratio v for $E/\sigma_{max} = 100$ (and $\sigma_y/\sigma_{max} = 1.0$) is also included in Fig. 8a (the range of v explored is found along the top horizontal axis). This clearly shows that v has little effect on K_{Ic}/K_0 and any variation can be neglected relative to the other dimensional groups.

Fig. 8b shows $K_{Ic}/K_0 = f(\sigma_y/\sigma_{max})$ for $E/\sigma_{max} = 50$, 100, 200 and 500. As in the upper curve of Fig. 7, each data point in this curve originates from a single calculation. This plot clearly shows that there is a slight variation in K_{Ic}/K_0 due to Young's modulus for $(\sigma_y/\sigma_{max})_{cr} < \sigma_y/\sigma_{max} < 2$. However, the two asymptotes remain unaffected (recall that there is one horizontal asymptote for large values of $\sigma_y/\sigma_{max} \to \infty$ and another for $\sigma_y/\sigma_{max} \to (\sigma_y/\sigma_{max})_{cr}$). All curves converge to the elastic solution for $\sigma_y/\sigma_{max} \to \infty$, and $(\sigma_y/\sigma_{max})_{cr}$ does not seem to be influenced by Young's modulus, E (as indicated by the convergence of all the curves to the same vertical asymptote for $\sigma_y/\sigma_{max} \to (\sigma_y/\sigma_{max})_{cr}$). Consequently, E/σ_{max} can be neglected in Eq. (8) (and in Eq. (11)).

4.3. Role of the characteristic lengths δ_n/λ and l_{cz}/λ in the crack behavior

The dimensional analysis performed in Section 2.6 identified the normalized critical opening displacement (δ_n/λ) as one of the dimensionless groups that may affect K_{Ic}/K_0. As discussed earlier, there are different ways to capture the influence of this parameter on crack behavior using other characteristic lengths. For example, l_{cz}/λ, which is the normalized cohesive zone length, and Γ_p/λ, which is used as an estimate of the size of the plastic zone around the crack tip for small-scale yielding problems (in this case, normalized with the wavelength of the sinusoidal interface) are possibilities. Since our intention is to focus on the characteristic length related to the intrinsic fracture behavior of the interface, and because the plastic zone size is also captured by $\sigma_y/\sigma_{max} \propto (l_{cz}/\Gamma_p)^{1/2}$, we chose to use the normalized cohesive zone length, l_{cz}/λ. Although l_{cz} is defined for the elastic case, this quantity can still be used as a measure of the fracture zone for small-scale yielding conditions and offers the advantage of allowing a more intuitive and meaningful analysis than simply using δ_n/λ alone. It is easier to compare the length over which the fracture mechanisms play an active role along the interface with the wavelength of the sinusoid (for example). For completeness, the plastic zone size is also included in this analysis to explore the different characteristic lengths, and their interaction, and how they affect the overall fracture behavior.

The crack evolution (which is the normalized crack tip position x/λ as a function of the applied load, K_I/K_0) is shown in the inset of Fig. 9a. Clearly, the cohesive zone length l_{cz}/λ affects both K_{init}/K_0 and K_{Ic}/K_0. Since we

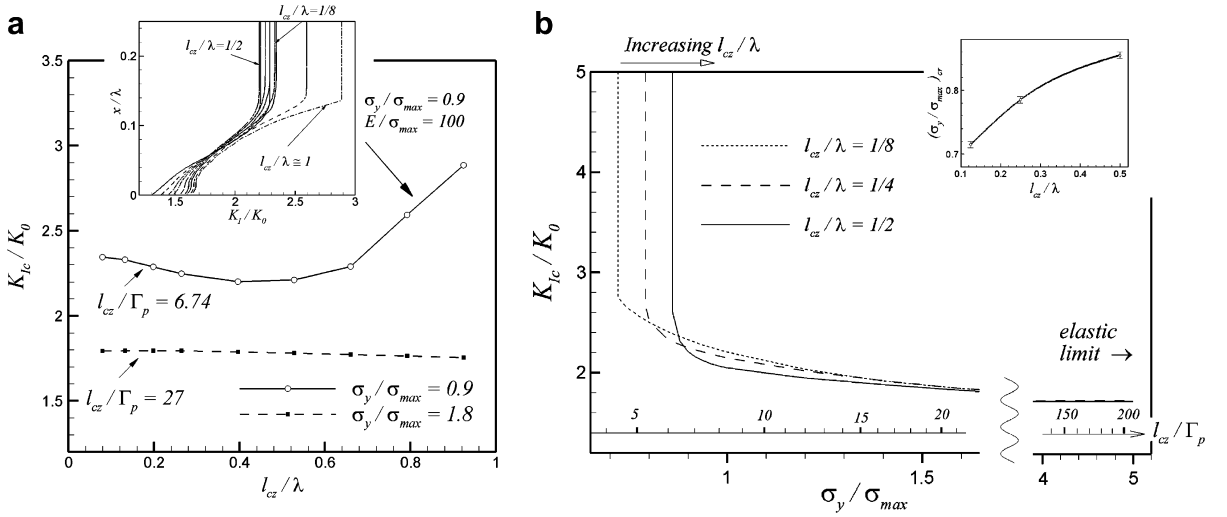

Fig. 9. (a) Effect of l_{cz}/λ for two values of $\sigma_y/\sigma_{\max} = 0.9$ and 1.8 (for $E/\sigma_{\max} = 100$ and $\nu = 0.3$). The enclosed figure shows an example of the effect of the cohesive zone length on crack evolution. (b) Effect of l_{cz}/λ on the $K_{Ic}/K_0 = f(\sigma_y/\sigma_{\max})$ curve clearly shows that there is a shift in the critical yield stress $(\sigma_y/\sigma_{\max})_{cr}$. The calculation presented in this figure correspond to an aspect ratio of $A/\lambda = 0.5$.

are essentially interested in the instability point, the main plot in Fig. 9a shows the influence of l_{cz}/λ on K_{Ic}/K_0 for two different values of $\sigma_y/\sigma_{\max}$ (=0.9 and 1.8). Those values of yield stress also have unique equivalents in terms of l_{cz}/Γ_p (= 6.74 and 27, respectively). The cohesive zone length spans from 0 to the sinusoid wavelength ($0 \leqslant l_{cz} \leqslant \lambda$); this guarantees that the fracture zone is still smaller than the actual interface wavelength. The maximum difference is observed for $\sigma_y/\sigma_{\max} = 0.9$ (or $l_{cz}/\Gamma_p = 6.74$) where a jump in K_{Ic}/K_0 of approximately 23% can be achieved by selecting the right material parameters. This result suggests that the variation of the cohesive zone length l_{cz}/λ has more influence on K_{Ic}/K_0 for those cases where both characteristic lengths compete with each other ($l_{cz} \approx \Gamma_p$) (this is appropriate for the lower values of $\sigma_y/\sigma_{\max}$). However, it is observed that for $l_{cz}/\lambda \approx 0.5$, K_{Ic}/K_0 shows a minimum. The drop is only about 5% with respect to the value of K_{Ic}/K_0 for $l_{cz}/\lambda \to 0$ compared with the gain of 23% when we increase $l_{cz}/\lambda \to 1$. We surmise that this minimum is primarily caused by the interaction between the cohesive zone and plastic zone when their sizes become similar. The manifestation of this minimum is not seen when plastic deformation is insignificant. In fact, when $l_{cz} \gg \Gamma_p$, l_{cz}/λ has a diminishing influence. Further study of this phenomenon is recommended if this becomes critical for the design of a tougher interface and the material and interface parameters are fixed and the only design variable is, for instance, the wavelength of the interface. The dashed curved for $\sigma_y/\sigma_{\max} = 1.8$ shows little variation with respect to l_{cz}/λ. This is consistent with the behavior observed for the purely elastic material [27] in which the cohesive zone length only affected the crack initiation, but did not have any influence on the macroscopic interface toughness. A better understanding on how l_{cz}/λ affects the crack behavior can be acquired from Fig. 9b where $K_{Ic}/K_0 = f(\sigma_y/\sigma_{\max})$ curves for three different values of l_{cz}/λ (= 1/8, 1/4 and 1/2) are plotted. As in previous cases, each data point along these curves is derived from individual calculations. The abscissa is defined by both, $\sigma_y/\sigma_{\max}$ and l_{cz}/Γ_p (upper horizontal axis) for comparison purposes. On the one hand, it can be seen that $(\sigma_y/\sigma_{\max})_{cr}$ is shifted to lower values (up to 10%) as l_{cz}/λ decreases. The inset figure shows the variation of $(\sigma_y/\sigma_{\max})_{cr}$ as a function of l_{cz}/λ. This indicates that l_{cz}/λ must be included in Eq. (11). Conversely, the existence of a critical characteristic length $(l_{cz}/\lambda)_{cr}$ for the transition from brittle to ductile crack propagation can be easily demonstrated. Consider the case of $\sigma_y/\sigma_{\max} = 0.8$, where $l_{cz}/\lambda = 1/4$. Crack evolution may become unstable because $\sigma_y/\sigma_{\max} = 0.8 > (\sigma_y/\sigma_{\max})_{cr}$ for $l_{cz}/\lambda = 1/4$ (corresponding to regimes III/IV in Fig. 9b). However, for $l_{cz}/\lambda = 1/2$, the crack behavior is ductile (since $\sigma_y/\sigma_{\max} = 0.8 < (\sigma_y/\sigma_{\max})_{cr}$, we are on the left portion of that curve in region IV). This indicates that $(l_{cz}/\lambda)_{cr}$ is indeed between $l_{cz}/\lambda = 1/4$ and 1/2. In order to obtain an accurate number for $(l_{cz}/\lambda)_{cr}$ more calculations are needed, and as discussed before, it should be anticipated that this will be somehow affected by the

other variables as well. Therefore, we anticipate that an expression similar to Eq. (11) will be needed for $(l_{cz}/\lambda)_{cr}$. This shows the benefit of increasing l_{cz}/λ for a fixed aspect ratio. The more the curve of Fig. 9b is shifted to the right, the more the regime IV can be maximized. Note that the level of improvement by inducing ductile behavior in this manner is more significant than the reduction in K_{Ic}/K_0 due to the local minimum observed in Fig. 9a when $l_{cz} \approx \Gamma_p$.

On the other hand, the three curves in the main figure tend asymptotically to the elastic solution for large values of σ_y/σ_{max}, or when $l_{cz} \gg \Gamma_p$, which means that the size of the plastic zone can be neglected relative to the fracture zone. The minimal influence of l_{cz}/λ on the macroscopic interface toughness may suggest that l_{cz}/λ can be eventually neglected in Eq. (8).

4.4. Role of sinusoidal interface geometry: A/λ

In Sections 4.1–4.3, we evaluated the material related parameters for a sinusoidal interface on the fracture behavior (macroscopic interface toughness and brittle-to-ductile transition) for a fixed aspect ratio. It was shown that K_{Ic}/K_0 for an elastic-perfectly plastic material departs from the straight crack solution [40,41]. We also showed how plasticity helps to increase K_{Ic}/K_0 relative to the elastic solution in [27]. An increase in K_{Ic}/K_0 is possible by tailoring specific material and interface cohesive parameters. We next focus on the effect of modifying the interface geometry on the fracture toughness for fixed material and cohesive parameters. Specifically, we wish to explore $K_{Ic}/K_0 = f(A/\lambda)$. We will then proceed to look at both material/interface parameters and interface geometry as we continue to develop Eq. (8).

We first consider the case with the following material parameters: $E/\sigma_{max} = 100$, $\nu = 0.3$, $\sigma_y/\sigma_{max} = 1$ and $l_{cz}/\lambda = 1/4$. Calculations for $A/\lambda = 0$, 0.05, 0.1, 0.2, 0.3, 0.4, 0.5, 0.6, 0.7, 0.8, 0.9, 1.0, 1.2, 1.5, 1.8 and 2.0 were carried out to explore how the crack growth deviates from a planar crack. The crack tip position as a function of the normalized applied load K_I/K_0 for each A/λ is shown in Fig. 10a. The macroscopic interface toughness, K_{Ic}/K_0, increases monotonically with increasing A/λ. Unstable crack propagation is delayed for steeper sinusoids up to $A/\lambda = 0.7$. The crack growth then "jumps" to a crack blunting regime (see Fig. 6d) wherein no instability is observed. From that point onwards, higher forces are required to propagate the crack as A/λ increases, generating more plastic deformation that resists crack growth. On the other hand, for $A/\lambda \to 0$ (i.e. planar interface), K_{Ic}/K_0 approaches the intrinsic toughness of the interface (which is expected for a straight crack along a planar interface). Note that the crack initiation point K_{init}/K_0 is also delayed as A/λ

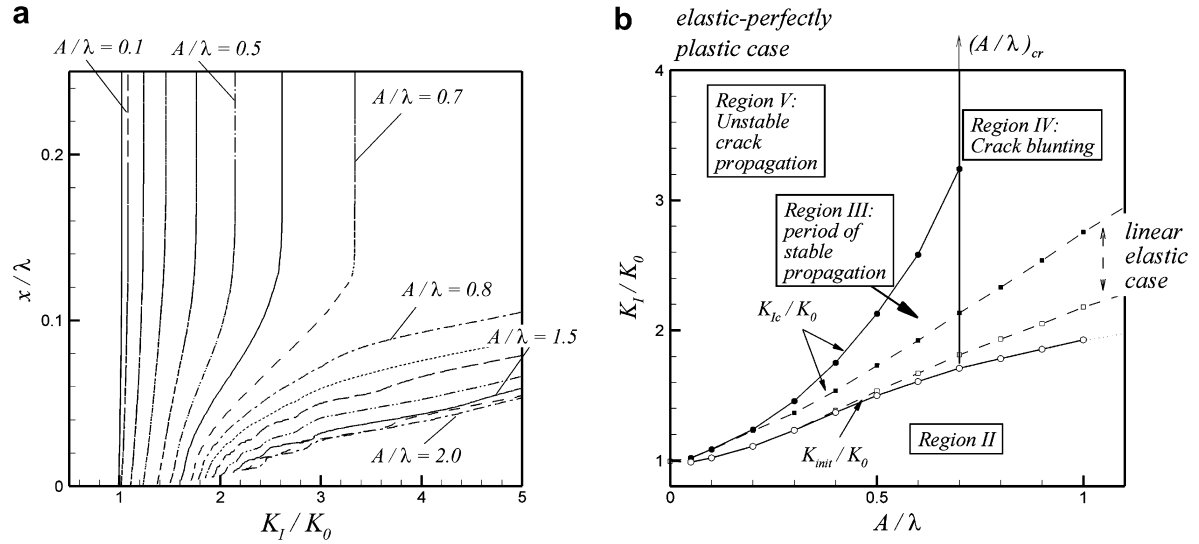

Fig. 10. (a) Crack evolution considering various aspect ratios, A/λ, for a given set of fixed material parameters ($\sigma_y/\sigma_{max} = 1.0$, $E/\sigma_{max} = 100$, $\nu = 0.3$ and $l_{cz}/\lambda = 1/4$). (b) Mapping of the regions of the different crack evolution behaviors, as a function of the aspect ratio. K_{init}/K_0 and K_{Ic}/K_0 delimit the regions II, III and V, whereas for $A/\lambda \geqslant 0.7$ define region IV where crack blunting produces stable crack propagation. The elastic case is shown in gray for comparison purposes.

increases. The location of the initial crack tip moves slightly (that is why a vertical shifting is observed in x/λ at crack initiation) which is the apparent crack advance by plastic flow at the blunted crack tip. No interface separation takes place until the first point in the curves indicates that the region near the crack tip undergoes large plastic deformation even before the crack starts growing. Alternatively, the crack moves because the material flows plastically.

In Fig. 10b, K_{init}/K_0 and K_{Ic}/K_0 are plotted as a function of A/λ. Each pair of points (i.e. each vertically-aligned K_{init}/K_0 and K_{Ic}/K_0 point) represents an individual calculation from Fig. 10a. This plot offers a mapping of the regions of the different crack growth behaviors. What is different from Fig. 7 is that the abscissa is now the aspect ratio, A/λ. Note that K_{init}/K_0 and K_{Ic}/K_0 delimit the regimes II, III and V for $A/\lambda \leqslant 0.7$. Regime IV, where crack blunting induces stable crack propagation, coincides with $A/\lambda > 0.7$. This suggests the existence of a critical aspect ratio, $(A/\lambda)_{\text{cr}}$, that denotes a sharp boundary between stable and unstable crack propagation and crack blunting. Hence, for a given set of material parameters, it is possible to control the crack growth behavior through $(A/\lambda)_{\text{cr}}$. If crack blunting is desired, then $A/\lambda > (A/\lambda)_{\text{cr}}$. Otherwise, if $A/\lambda < (A/\lambda)_{\text{cr}}$, brittle crack evolution is predicted. Note that $(A/\lambda)_{\text{cr}}$ lies between $0.7 < (A/\lambda)_{\text{cr}} < 0.8$. An accurate determination $(A/\lambda)_{\text{cr}}$ will require the creation of additional models with aspect ratios in the $A/\lambda = 0.7 - 0.8$ range. This is very important for those cases mentioned before, where manipulating material properties has a diminishing return and the only way to improve cohesion is by modifying the geometry of the interface as Fig. 10b suggests.

Another interesting characteristic of the curves in Fig. 10b is that K_{Ic}/K_0 changes more rapidly than K_{init}/K_0 as A/λ is increased. This expands region III (i.e. the of stable crack propagation regime) with respect of A/λ (for $A/\lambda \leqslant (A/\lambda)_{\text{cr}}$). The elastic case is shown in gray for comparison purposes. The crack initiation limit did not change significantly from the elastic case. However, it is observed that the instability curve (i.e. the curve corresponding to K_{Ic}/K_0) is considerably different. While $K_{\text{Ic}}/K_0 = f(A/\lambda)$ fits a linear function for the elastic case (see Fig. 4), the elastic-perfectly plastic case follows a quadratic function of the form:

$$\frac{K_{\text{Ic}}}{K_0} \approx 1 + 4.37\left(\frac{A}{\lambda}\right)^2, \quad \text{for } A/\lambda \leqslant (A/\lambda)_{\text{cr}} \tag{12}$$

where $E/\sigma_{\max} = 100$, $\nu = 0.3$, $\sigma_y/\sigma_{\max} = 1$ and $l_{cz}/\lambda = 1/4$. Eq. (12) was obtained from a fit to the upper curve in Fig. 10b. It is expected that the constant multiplier in Eq. (12) will change for other material parameters. Eq. (12) is just one step forward to obtaining a more comprehensive look at the nature of Eq. (8). The other influential parameters such as $\sigma_y/\sigma_{\max}$ and l_{cz}/λ should also be included as previously discussed. The coupling between all of these variables will be discussed next.

4.4.1. Coupling with the normalized yield stress

The details in Sections 4.1–4.3 suggest that $\sigma_y/\sigma_{\max}$ plays the most influential role (of the different material parameters) on crack behavior. In order to evaluate possible coupling between $\sigma_y/\sigma_{\max}$ and A/λ, several calculations were carried out for all meshes and $\sigma_y/\sigma_{\max} = 0.5$, 1.0, 2.0, 3.0 and 5.0. The other material parameters remained unchanged, i.e. $E/\sigma_{\max} = 100$, $\nu = 0.3$ and $l_{cz}/\lambda = 1/4$. Fig. 11 shows the $K_{\text{Ic}}/K_0 = f(A/\lambda)$ curve for each $\sigma_y/\sigma_{\max}$ including the limiting elastic case $\sigma_y/\sigma_{\max} \to \infty$. As previously mentioned, we will mainly focus on the instability point rather than the crack initiation point, and hence we do not show the crack initiation load K_{init}/K_0 from this point onwards. It should be noted that any of these equations can be fitted with polynomials as illustrated with Eq. (12). For lower values of $\sigma_y/\sigma_{\max}$ (= 0.5, 1.0 and 2.0), the critical aspect ratios to induce crack blunting (i.e. the transition from regimes III/V to IV in Fig. 10b) are labeled as $(A/\lambda)^{0.5}_{\text{cr}}$, $(A/\lambda)^{1.0}_{\text{cr}}$ and $(A/\lambda)^{2.0}_{\text{cr}}$, respectively. Fig. 11 shows that the critical aspect ratio increases as $\sigma_y/\sigma_{\max}$ increases. However, no transition is observed for $\sigma_y/\sigma_{\max} \geqslant 3.0$ for any of the meshes. This suggests that there is a strong coupling between A/λ and $\sigma_y/\sigma_{\max}$, and the definition of the critical normalized yield stress or critical aspect ratio is very much dependent upon how the problem is formulated. In fact, a designer could find $(\sigma_y/\sigma_{\max})_{\text{cr}}$ using Fig. 7 if A/λ is fixed, or alternatively, find the $(A/\lambda)_{\text{cr}}$ using Figs. 10b or 11 if $\sigma_y/\sigma_{\max}$ is fixed. In other words, an expression analogous to Eq. (11) can be established that relates the critical aspect ratio to the key material parameters. For example,

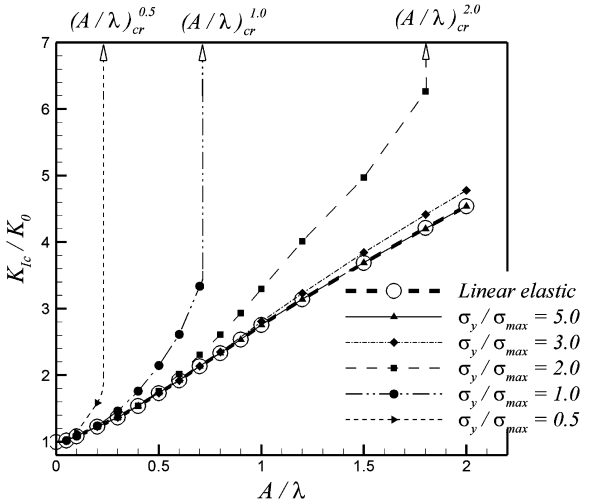

Fig. 11. Interface fracture toughness as a function of the aspect ratio for various values of σ_y/σ_{max}. The critical aspect ratios $(A/\lambda)_{cr}$ were taken from Fig. 12b. The other material parameters considered in this analysis are $E/\sigma_{max} = 100$, $\nu = 0.3$ and $l_{cz}/\lambda = 1/4$.

$$\left(\frac{A}{\lambda}\right)_{cr} = \Phi\left(\frac{\sigma_y}{\sigma_{max}}, \frac{E}{\sigma_{max}}, \nu, n, \frac{l_{cz}}{\lambda}\right) \tag{13}$$

This can also be explored from another viewpoint if the relationship $K_{Ic}/K_0 = f(\sigma_y/\sigma_{max})$ is analyzed for different values of A/λ. This is shown in Fig. 12a (for $E/\sigma_{max} = 100$, $\nu = 0.3$ and $l_{cz}/\lambda = 1/4$). As in previous cases, each data point is obtained from individual calculations. The empty circles denote the critical normalized yield stress $(\sigma_y/\sigma_{max})_{cr}$ for each value of A/λ. As was the case for $A/\lambda = 0.5$ in Section 4.1, each one of these curves displays two asymptotes. The horizontal asymptote to $\sigma_y/\sigma_{max} \to \infty$ suggests that the macroscopic toughness, K_{Ic}/K_0, tends to that for an elastic solid [27]. The vertical asymptote for $\sigma_y/\sigma_{max} \to (\sigma_y/\sigma_{max})_{cr}$ where $K_{Ic}/K_0 \to \infty$, denotes the onset of crack blunting due to plasticity.

Fig. 12a suggests a clear relationship between$(\sigma_y/\sigma_{max})_{cr}$ and $(A/\lambda)_{cr}$ which is captured in Fig. 12b. This plot shows values of $(\sigma_y/\sigma_{max})_{cr}$ taken directly from Fig. 12a indicating two distinct crack regimes. These are divided by the solid curve defined as $(\sigma_y/\sigma_{max})_{cr} = f\{(A/\lambda)_{cr}\}$ which, surprisingly, happens to follow a linear relationship and serves to connect Eqs. (11) and (13). The upper region labeled as "Crack instability" denotes

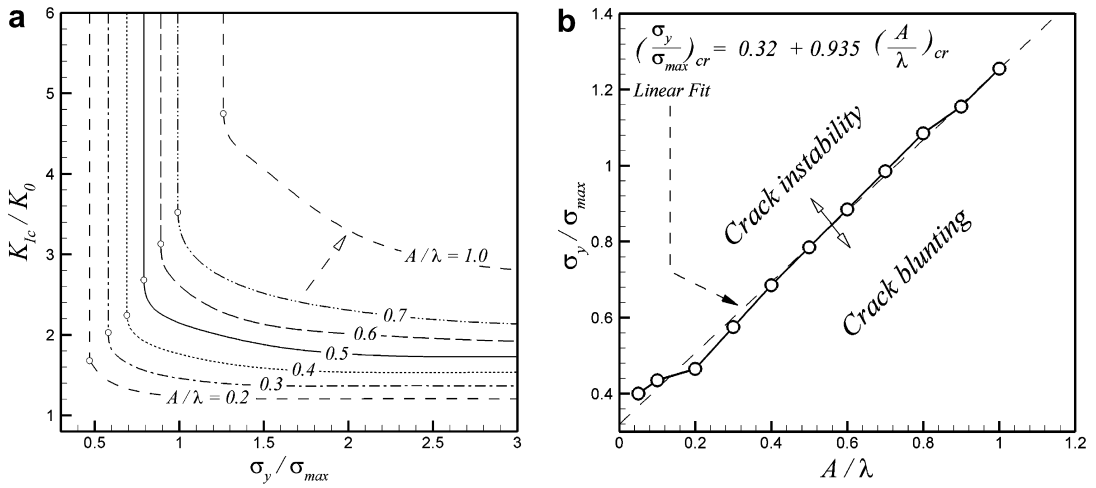

Fig. 12. (a) $K_{Ic}/K_0 = f(\sigma_y/\sigma_{max})$ for different values of A/λ. The empty circles denote $(\sigma_y/\sigma_{max})_{cr}$. (b) $(\sigma_y/\sigma_{max})_{cr}$ vs. $(A/\lambda)_{cr}$. The solid line defines the boundary between the brittle and ductile behaviors. The other material parameters considered in this analysis are $E/\sigma_{max} = 100$, $\nu = 0.3$ and $l_{cz}/\lambda = 1/4$.

brittle behavior (for small-scale yielding) which results if sufficient load is applied. Alternatively, the region below the solid line in Fig. 12b corresponds to more ductile behavior leading to crack blunting. The implication of this analysis is that an analyst could potentially choose a given set of material properties or interface geometries to either increase fracture toughness in a brittle regime or induce a more ductile behavior. The interpolated values of $(A/\lambda)_{cr}$ used in Fig. 11 (defined with dotted lines for $\sigma_y/\sigma_{max} = 0.5$, 1.0 and 2.0) have been taken directly from Fig. 12b.

4.4.2. Coupling with the other material parameters

An analysis of the influence of E/σ_{max} and l_{cz}/λ on $K_{Ic}/K_0 = f(A/\lambda)$ (upper curve of Fig. 10b) was also conducted. Consistent with the findings of Section 4.2, Young's modulus effect can be neglected. In addition to this, it is observed that the critical aspect ratio to induce ductile crack blunting $(A/\lambda)_{cr}$ is not affected by E/σ_{max}, which is also consistent with the fact that $(\sigma_y/\sigma_{max})_{cr}$ is independent of E/σ_{max}. In the same way, K_{Ic}/K_0 is somewhat insensitive to changes in l_{cz}/λ, except for $(A/\lambda)_{cr}$, where there is a variation of about 10% when the cohesive zone length is halved or doubled. A consequence of these variables is that, for example, the upper curve of Fig. 10b may have a shift for other values of l_{cz}/λ (or δ_n/λ), but would remain the same for any variation of E/σ_{max}. Since the influence of these parameters on the upper curve of Fig. 10b is very small, we did not include any figure illustrating this analysis.

4.4.3. Influence of the shape of the constitutive cohesive law

Up to this point, we have considered the influence of the dimensionless groups containing the cohesive strength σ_{max}, work of separation ϕ_n and its cohesive zone length l_{cz}. However, these results have been obtained using Eq. (5). Since the influence of the actual shape of the cohesive law on fracture behavior of interfaces has been long under debate [29], separate analyses of other constitutive cohesive laws were conducted to ensure that the developments in Section 4 still hold provided that the main cohesive parameters are retained.

In addition to the Xu–Needleman law shown in Fig. 1 (Eq. (5)), we also investigated laws that follow trapezoidal and triangular shapes [29]. By holding the other dimensionless parameters constant, we found: for constant A/λ, the trapezoidal law predicts the same $(\sigma_y/\sigma_{max})_{cr}$ and same K_{Ic}/K_0 (for the elastic limit, $\sigma_y/\sigma_{max} \to \infty$) as the Xu–Needleman law. However, the triangular law predicts a value of$(\sigma_y/\sigma_{max})_{cr}$ with an error of approximately 10% with respect to the results obtained with the trapezoidal and Xu–Needleman laws for $A/\lambda = 0.5$. On the other hand, the trapezoidal law showed a significant change in the elastic limit for K_{Ic}/K_0 when the initial stiffness of the cohesive law (the elastic region of the cohesive law for $\sigma < \sigma_{max}$ and $\Delta_n \leqslant \delta_{peak}$) was decreased considerably so as to affect the overall compliance of the interface. If such constitutive cohesive laws are used, we recommend including the initial stiffness of the cohesive law as another design parameter. A thorough study of the effect of cohesive laws on variations of relevant cohesive parameters is beyond the scope of this work. However, this study enabled us to conclude that the results in this section indicate that the actual shape of the constitutive cohesive law is of secondary importance to the major developments in this work.

5. Interface toughness prediction for elastic–plastic materials with hardening

As noted in other work, the effect of hardening on the fracture toughness of interfaces can be quite significant [40,41]. In this section, we analyze how the crack propagation behavior considered in Section 4 for an elastic-perfectly plastic material is affected when the material strain hardens. From Eq. (1), the hardening is characterized by the hardening exponent n. The higher this parameter, the more the material hardens as it is strained. Hardening will inhibit ductility and enhance conditions for unstable crack propagation. Therefore, it is important to understand those conditions and make the necessary correction to the mappings established by Figs. 7 and 10b.

The first numerical test evaluates how the crack propagation behavior varies when the strain-hardening exponent increases from $n = 0$ for two representative cases: (1) when the elastic-perfectly plastic material develops crack blunting, $\sigma_y/\sigma_{max} < (\sigma_y/\sigma_{max})_{cr}$; (2) when the conditions for crack blunting are not given by $\sigma_y/\sigma_{max} > (\sigma_y/\sigma_{max})_{cr}$. For both cases, calculations were carried out for $E/\sigma_{max} = 100$, $\nu = 0.3$, $l_{cz}/\lambda = 1/4$ and $A/\lambda = 0.5$ increasing n from 0 to 0.3. Recall that for this particular set of parameters, $(\sigma_y/\sigma_{max})_{cr} \approx 0.78$.

Fig. 13a shows the variation of K_{Ic}/K_0 as a function of n for case 1 with $\sigma_y/\sigma_{max} = 0.7$ and case 2 with $\sigma_y/\sigma_{max} = 1.0$. The inset figure shows the crack evolution for several values of n for the case where there is crack blunting at $n = 0$. As n increases, the load required to propagate the crack diminishes until a critical value n_{cr} is reached at which point the crack becomes unstable for $n \geqslant n_{cr}$. After that point, K_{Ic}/K_0 can be defined by the vertical line in the crack evolution curve and it is seen that this toughness decreases as n is further increased. The main plot in Fig. 13a shows $K_{Ic}/K_0 = f(n)$, in which the vertical line indicates the critical strain-hardening exponent n_{cr} (which is $n_{cr} = 0.05$ for this particular set of parameters). In contrast, for $\sigma_y/\sigma_{max} = 1.0 > (\sigma_y/\sigma_{max})_{cr}$, K_{Ic}/K_0 does not appear to vary significantly with respect to n (compared with the first case). However, a change of about 10% results from changing $n = 0$ to 0.3.

5.1. Relationship between toughness, n and σ_y/σ_{max}

To further analyze the coupling between n and σ_y/σ_{max}, additional calculations were carried out in order to find an explicit form for $K_{Ic}/K_0 = f(\sigma_y/\sigma_{max})$ for different values of n. Fig. 13b shows the case for $n = 0$ (see Fig. 7) as a solid line and the effect of the hardening exponent for $n = 0.1$ and 0.2. The empty circles denote values of $(\sigma_y/\sigma_{max})_{cr}$ (vertical asymptote). It is interesting that $(\sigma_y/\sigma_{max})_{cr}$ varies significantly with n. In fact, the values are $(\sigma_y/\sigma_{max})_{cr} = 0.78$, 0.61 and 0.37, for $n = 0$, 0.1 and 0.2, respectively. This represents a reduction of about 40% with respect to the original results reported in Section 4.1 for a material with $n = 0.2$. It is evident from these plots that strain-hardening indeed facilitates the conditions for more brittle behavior, making selection of the right material parameters for maximum interface toughness more challenging for a fixed interface geometry. It should be expected that $(\sigma_y/\sigma_{max})_{cr} \to 0$ for the limiting case of $n \to 1$ (the elastic case).

Another important observation is that we can also look at the dependence of n_{cr} on σ_y/σ_{max} (similar to our discussion around the dependence of $(\sigma_y/\sigma_{max})_{cr}$ on n). This can be observed in Fig. 13b. For any $\sigma_y/\sigma_{max} < 0.785$, it is possible to find a value of n_{cr} such that crack evolution transitions from blunting to unstable propagation. Consider the case of $\sigma_y/\sigma_{max} = 0.7$ and $n = 0$: crack evolution is stable with blunting. However, for $n = 0.1$ the crack behavior is brittle (since we are on the right portion of the curve in region V). This indicates that n_{cr} indeed falls between $n = 0$ and $n = 0.1$ (in fact $n_{cr} = 0.05$ as shown in Fig. 13a for this particular set of parameters). If $\sigma_y/\sigma_{max} = 0.5$ is assumed, one can infer that n_{cr} is indeed between $n = 0.1$ and $n = 0.2$. Conversely, values of $\sigma_y/\sigma_{max} \geqslant 0.785$ would not yield any meaningful value of n_{cr} unless a material with softening ($n < 0$) is considered (which is outside the scope of this work).

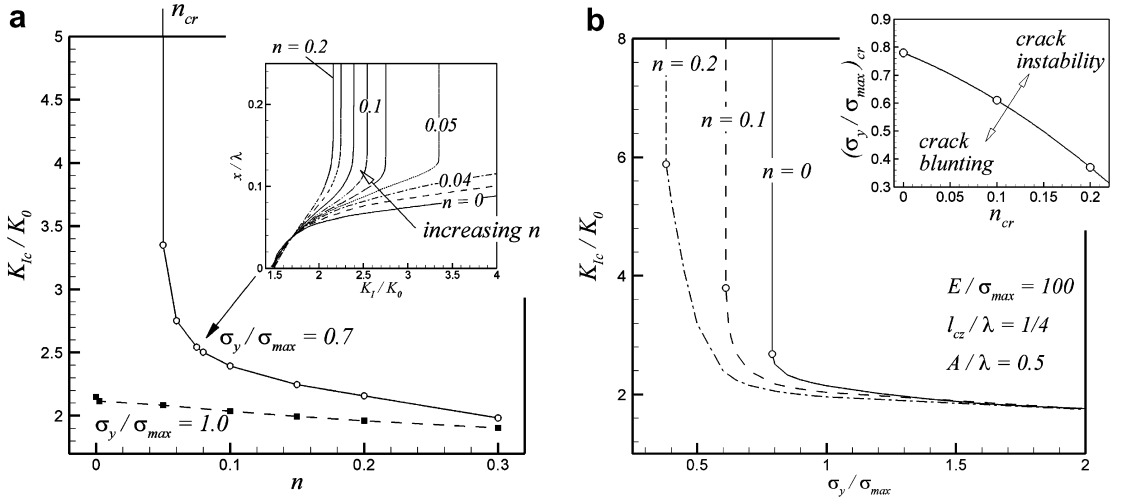

Fig. 13. (a) Effect of the hardening for $A/\lambda = 0.5$, $E/\sigma_{max} = 100$, $v = 0.3$ and $l_{cz}/\lambda = 1/4$. $K_{Ic}/K_0 = f(n)$ for two different σ_y/σ_{max}. The inset figure shows the crack evolution for $\sigma_y/\sigma_{max} = 0.7$ that indicates that there is a critical n_{cr}, such that there is crack blunting if $n < n_{cr}$. (b) Effect of the hardening for $A/\lambda = 0.5$, $E/\sigma_{max} = 100$, $v = 0.3$ and $l_{cz}/\lambda = 1/4$. $K_{Ic}/K_0 = f(\sigma_y/\sigma_{max})$ for different values of n. The empty circles denote the $(\sigma_y/\sigma_{max})_{cr}$. The inset figure shows the relationship between $(\sigma_y/\sigma_{max})_{cr}$ and n_{cr}.

Not surprisingly, a unique relationship $(\sigma_y/\sigma_{\max})_{cr} = f(n_{cr})$ can be posed (as was the case for $(A/\lambda)_{cr}$). This would in principle give a designer the flexibility to pick one or another variable depending upon which of these two material parameters is easier to modify for a fixed aspect ratio. This relationship is plotted in the inset plot of Fig. 13b indicating those regions where crack blunting and unstable crack growth regimes (or equivalently, brittle or ductile, respectively) can take place. While knowledge of $(\sigma_y/\sigma_{\max})_{cr} = f(n_{cr})$ contributes directly to Eq. (11), the inverse $n_{cr} = f(\sigma_y/\sigma_{\max})$ suggests that there has to be a new expression similar to Eqs. (11) and (13) for n_{cr}. Consideration of the aspect ratio as a design variable for hardening materials is discussed next.

5.2. Relationship between toughness, n and A/λ

The possibility of increasing K_{Ic}/K_0 by modifying A/λ remains to be evaluated. Starting from $n = 0$ and $\sigma_y/\sigma_{\max} = 1.0$, $E/\sigma_{\max} = 100$, $\nu = 0.3$ and $l_{cz}/\lambda = 1/4$, $K_{Ic}/K_0 = f(A/\lambda)$ is investigated for two additional strain-hardening exponents, namely $n = 0.1$ and 0.2. Fig. 14 shows the variation of the macroscopic interface toughness K_{Ic}/K_0 with A/λ and how the critical aspect ratio to induce crack blunting, $(A/\lambda)_{cr}$, is significantly affected by the hardening exponent. For this particular set of parameters, $(A/\lambda)_{cr} \approx 0.7$, 1.0 and 1.2, for $n = 0$, 0.1 and 0.2, respectively (these values are indicated in Fig. 14). As previously discussed, an accurate determination of these values will require more meshes. It is clear from this analysis that the effect of hardening makes it more difficult to find a suitable aspect ratio to either increase K_{Ic}/K_0 or to induce crack blunting. In fact, increasing n narrows the region of crack blunting (regime IV) as illustrated in Fig. 10b. We note that the effect of hardening becomes more prominent at larger A/λ. For fixed A/λ, K_{Ic}/K_0 decreases with increasing n suggesting an increased tendency toward brittle fracture.

Following the line of reasoning that led us to conclude the existence of $(A/\lambda)_{cr}$, we can similarly explore how n_{cr} is affected by A/λ. The inset in Fig. 14 shows $(A/\lambda)_{cr} = f(n_{cr})$. The same plot indicates regimes of brittle and ductile behavior depending on the specific values of A/λ and n. However, since n_{cr} is also a function of $\sigma_y/\sigma_{\max}$, it is anticipated that the inset in Fig. 14 will be different for other values of $\sigma_y/\sigma_{\max}$. It is therefore possible to express this critical hardening exponent, n_{cr}, as

$$n_{cr} = \psi\left(\frac{\sigma_y}{\sigma_{\max}}, \frac{E}{\sigma_{\max}}, \nu, \frac{l_{cz}}{\lambda}, \frac{A}{\lambda}\right). \tag{14}$$

Although the dependence of n_{cr} with respect to the elastic parameters and the characteristic lengths is not evaluated explicitly, we do not expect significant variations with respect to $E/\sigma_{\max}$, ν or l_{cz}/λ.

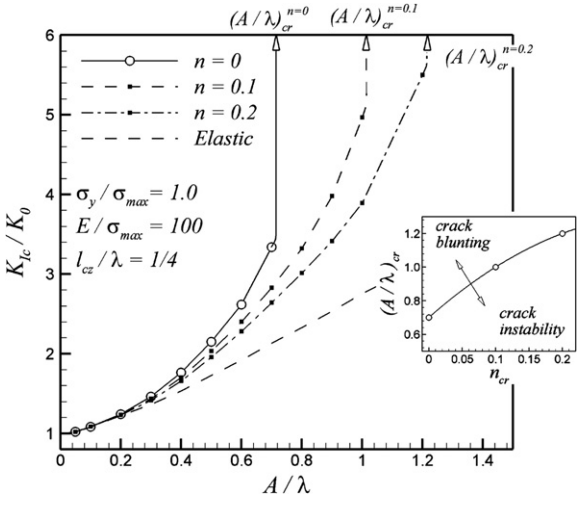

Fig. 14. $K_{Ic}/K_0 = f(A/\lambda)$ for different values of n. The inset figure shows the relationship between $(A/\lambda)_{cr}$ and n_{cr}.

6. Discussion of the results

In the course of developing the above relations, some new physics was revealed which is now summarized:

1. Three different types of crack evolution behavior were described. Type 1 occurs when the crack runs through a small portion of the sinusoidal interface in a stable fashion and then reaches the critical load at which it becomes unstable (brittle behavior). Type 2 occurs when the crack keeps growing in a stable fashion with a considerable amount of plastic deformation around the crack tip and significant blunting (ductile behavior). Type 3 occurs when the crack does not grow. Transitions between the different types of behavior are contingent upon a set of critical values of key material and geometric parameters.
2. For those interface where the crack behaves as Type 1, the macroscopic interface toughness can be increased by decreasing the normalized yield stress $\sigma_y/\sigma_{\max}$ (as shown in Fig. 7), decreasing the hardening exponent n (Fig. 13b) or by increasing the aspect ratio A/λ (Fig. 10b). While increasing l_{cz}/λ (or δ_n/λ) or decreasing $E/\sigma_{\max}$ can also improve the interface toughness, their influence is far less significant.
3. The transition from an interface of Type 1 to Type 2 for fixed material parameters is characterized by a set of critical values of $\sigma_y/\sigma_{\max}$, n, l_{cz}/λ and A/λ. For instance, a larger aspect ratio suggests blunting, while a smaller aspect ratio suggests increased likelihood for instability. A linear relationship between the critical aspect ratio and similarly defined critical yield strength was established. It is expected, however, that this relationship will be influenced to a small degree by the characteristic length, slightly by the choice of the cohesive law, but greatly affected by the hardening exponent. This enables the development of maps for crack behavior for any given set of material parameters and aspect ratio.
4. A mapping of the different crack propagation regimes was presented in Figs. 7 and 10b where the critical material or geometrical parameters for the transition between the brittle or ductile behavior are well defined. The relationship between the critical aspect ratio and the critical normalized yield stress was plotted in Fig. 12b where the boundary between the two distinct types of behaviors is indicated. A similar relationship between the critical hardening exponent and the critical yield stress was also presented in the inset plot of Fig. 13b. Fig. 14 shows the relationship between the critical hardening exponent and the critical aspect ratio.

Although Eq. (8) was introduced to provide an indication of which material and geometric parameters might affect the macroscopic interface toughness, it is recognized that this relation is better described by a multi-dimensional (or hyper) surface given by:

$$\Theta\left[(A/\lambda)_{\mathrm{cr}}, (\sigma_y/\sigma_{\max})_{\mathrm{cr}}, n_{\mathrm{cr}}, (l_{cz}/\lambda)_{\mathrm{cr}}\right] = 0 \tag{15}$$

Brittle fracture results where

$$\Theta[A/\lambda, \sigma_y/\sigma_{\max}, n, l_{cz}/\lambda] < 0 \tag{16}$$

Ductile fracture occurs for

$$\Theta[A/\lambda, \sigma_y/\sigma_{\max}, n, l_{cz}/\lambda] > 0 \tag{17}$$

Eqs. (15)–(17) require further numerical evaluation. Evidently the selection of the sign in the inequalities of Eq. (16) and (17) is arbitrary, and the analyst should look at the relationships shown in Fig. 12b and in the inset of Figs. 13b and 14. Clearly, the results of the present effort demonstrate that incorporation of a plasticity material model results in a much richer physical problem which at the same time is substantially more complicated than its elastic counterpart.

7. Conclusions

The goal of this work was to explore the possibility of designing failure-resistant interfaces having a non-planar geometry. For this purpose, we selected a pure sinusoidal geometry that is described by its aspect ratio or ratio of amplitude to wavelength (i.e. a single geometric parameter). The key result from the present work is that the macroscopic interface toughness (and hence the extent to which a crack can grow freely, or have its

growth arrested) can be manipulated through suitable selection of the aspect ratio. However, toughness is also dependent upon the parameters associated with the plasticity material model. For the elastic material model, we found that relationship is linear for large values of A/λ and shows a clear tendency to the Griffith criterion $K_{Ic} \to K_0$ when $A/\lambda \to 0$ [27]. No dependence upon material parameters was found. This suggests that for fixed wavelength, increasing the peak-to-valley heights of the sinusoidal asperities effectively delays unstable crack growth in an elastic material. For the elastic–plastic material model, we identified a set of critical geometric and material parameters that govern the transition from brittle to ductile fracture. Selection of these parameters requires the evaluation of a multi-dimensional function that accounts for each parameter.

Regarding future extensions of the present methodology, a key deficiency of the present model is the absence of environmental effects (such as corrosion) on crack growth as well as interface response in fatigue. The response of a sinusoidal surface to shear (and combined) loading should be explored. Evidence from the work of Keisler and Lataillade [21] suggests that laser-textured [22] steel substrate surface morphologies lead to a dramatic increase in shear strength of adhesively bonded steel joints under dynamic loading conditions. In addition to the surface morphology pattern, we expect that plasticity of surface asperities (neglected in the present work) is likely to play a more prominent role in shear loading than in tension. Although dynamic loading conditions are not considered in the present methodology, it would be especially interesting to explore the effect of surface aspect ratio on interfacial toughening at high strain rates.

Acknowledgement

The authors are grateful to Jessica Schroeder for supplying several important references and for many stimulating discussions on the bonded interface topography design for toughness enhancement.

References

[1] Garnish EW, Haskins GC. In: Alner DJ, editor. Aspects of adhesion, vol. 5. University London Press Ltd.; 1969. p. 259.
[2] Sancaktar E, Zhang E. Laser ablation of aluminum and titanium surfaces for improved adhesion. In: Sancaktar E, Lee JS, editors. Reliability stress analysis and failure prevention aspects of composite and active materials, ASME DE, vol. 79. New York, NY: American Society of Mechanical Engineers; 1994. p. 65.
[3] Sancaktar E, Gomatam R. A study on the effects of surface roughness on the strength of single lap joints. J Adhesion Sci Technol 2001;15:97–117.
[4] Jennings CW. Surface roughness and bond strength of adhesives. J Adhesion 1972;4:25–38.
[5] Mulville DR, Vaishnev RN. Interfacial crack propagation. J Adhesion 1975;7:215.
[6] Stout KJ, Blunt L, Dong WP, Mainsah W, Luo N, Mathia T, et al. Development of methods for the characterization of roughness in three dimensions. Burlington, MA: Butterworth-Heineman; 2000.
[7] Hector Jr LG, Sheu S. Brightness enhancement with textured roll. US Patent No. 4,996,113, 1991.
[8] Hector Jr LG, Sheu S. Enhanced work roll surface texture for cold and hot rolling of aluminum and its alloys. US Patent No. 5,508,119, 1996.
[9] Sheu S, Hector Jr LG, Gorman Sr JM. Sheet product due to massive thickness reduction in last stand of cold rolling. US Patent No. 5,537,851, 1996.
[10] Sheu S, Hector Jr LG, Richmond O. Tool surface topographies for controlling friction and wear in metal-forming processes. ASME J Tribol 1998;120:517–27.
[11] Chandrasekhar S. Hydrodynamic and hydromagnetic stability. Oxford: Clarendon Press; 1961.
[12] Ciamarra MP, Coniglio A, Nicodemi M. Shear instabilities in granular mixtures. Phys Rev Lett 2005;94:188001.
[13] Chen EJ, Winn Z. Delaminating layered oxide composites with wavy interfaces. Z Metallkd 2001;7:757.
[14] Barthelat F, Tang H, Zavattieri PD, Li C-M, Espinosa HD. On the mechanics of mother-of-pearl: a key feature in the material hierarchical structure. J Mech Phys Solid 2007;55(2):306–37.
[15] Li JH, Yamaguchi Y, Hashizume H, Usami N, Shiraki Y. Wavy interface morphologies in strained Si1-xGex/Si multilayers on vicinal Si(111) substrates. J Phys: Condens Matter 1998;10:8643–52.
[16] Asaro RJ, Tiller WA. Interface morphology development during stress corrosion cracking. I. Via surface diffusion. Metall Trans 1972;3:1789–96.
[17] Mullins W, Sekerka RF. The stability of a planar interface during solidification of a dilute binary alloy. J Appl Phys 1964;35:444.
[18] Singh S, Blazek K. Heat transfer and skin formation in a continuous casting mold as a function of steel carbon content. J Met 1974;26:17–27.
[19] Weirauch DA, Giron A. The early stages of aluminum solidification in the presence of a moving meniscus. In: Zabaras N, Becker R, Lalli L, Ghosh S, editors. Proceedings of the integration of material, process and product design – a conference dedicated to the 70th birthday of Owen Richmond. Rotterdam, The Netherlands: A.A. Balkema Publishers; 1998. p. 183.

[20] Yigit F, Hector Jr LG. Critical wavelengths for gap nucleation in solidification – Part I: theoretical methodology. ASME J Appl Mech 2000;67:66–76.
[21] Yigit F, Hector Jr LG. Critical wavelengths for gap nucleation in solidification – Part II: results for selected mold-shell material combinations. ASME J Appl Mech 2000;67:77–86.
[22] Lu X, Comninu M. The sinusoidal crack. Engng Fract Mech 1989;34:649–56.
[23] Yang L, Qu J. Energy release rate for cracks on a non-planar interface. Key Engng Mater 1996;121–122:47–62.
[24] Cotterell B, Rice JR. Slightly curved or kinked cracks. Int J Fract 1980;16:155–69.
[25] Johnson KL, Greenwood JA, Higginson JG. The contact of elastic regular wavy surfaces. Int J Mech Sci 1985;27:383.
[26] Adams GG. Adhesion at the wavy contact interface between two elastic bodies. ASME J Appl Mech 2004;71:851–6.
[27] Zavattieri P, Hector Jr LG, Bower AE. Determination of the effective mode-I toughness of a sinusoidal interface between two elastic solids. Int J Fract 2007;145(3):167–80.
[28] Anderson TL. Fracture mechanics – fundamentals and applications. CRC Press; 1995.
[29] Chandra N, Li H, Shet C, Ghonem H. Some issues in the application of cohesive zone models for metal–ceramic interfaces. Int J Solid Struct 2002;39(10):2827–55.
[30] Qi Y, Hector Jr LG. Adhesion and adhesive transfer at aluminum/diamond interfaces: a first-principles study. Phys Rev B 2004;69:235401.
[31] Tijssens MGA, van der Giessen E, Sluys LJ. Simulation of mode I crack growth in polymers by crazing. Int J Solid Struct 2000;37:7307–27.
[32] Alfano G, Marfia S, Sacco E. Influence of water pressure on crack propagation in concrete dams. In: Neittaanmäki P, Rossi T, Majava K, Pironneau O, editors. Proceedings of the fourth European congress on computational methods in applied sciences and engineering. ECCOMAS2004. Jyväskylä, Finland; 2004.
[33] Xu X-P, Needleman A. Numerical simulations of fast crack growth in brittle solids. J Mech Phys Solid 1994;42(9):1397–434.
[34] van den Bosch MJ, Schreurs PJG, Geers MGD. An improved description of the exponential Xu and Needleman cohesive zone law for mixed-mode decohesion. Engng Fract Mech 2006;73(9):1220–34.
[35] Gao YF, Bower AF. A simple technique for avoiding convergence problems in finite element simulations of crack nucleation and growth on cohesive interfaces. Model Simul Mater Sci Engng 2004;12:453.
[36] ABAQUS, Version 6.4-1, HKS Inc., Providence, RI.
[37] Buckingham E. On physically similar systems; illustrations of the use of dimensional equations. Phys Rev 1914;4:345–76.
[38] Rice JR. The mechanics of earthquake rupture. In: Dziewonski AM, Boschi E, editors. Physics of the earth's interior. Italian Physical Society and North-Holland; 1980. p. 555–649.
[39] Irwin GR. Analysis of stresses and strains near the end of a crack traversing a plate. ASME J Appl Mech 1957;24:361–4.
[40] Tvergaard V, Hutchinson JW. The relation between crack growth resistance and fracture process parameters in elastic–plastic solids. J Mech Phys Solid 1992;40:1377–97.
[41] Tvergaard V, Hutchinson JW. The influence of plasticity on mixed mode interface toughness. J Mech Phys Solid 1993;41:1119–35.
[42] Mediavilla J, Peerlings RHJ, Geers MGD. A robust and consistent remeshing-transfer operator for ductile fracture simulations. Comput Struct 2006;84(8-9):604–23.
[43] Li SF, Liu WK, Rosakis AJ, Belytschko T, Hao W. Mesh-free Galerkin simulations of dynamic shear band propagation and failure mode transition. Int J Solid Struct 2002;39(5):1213–40.
[44] Rice R, Drugan WJ, Sham T-L. Elastic–plastic analysis of growing cracks. In: Proceedings of fracture mechanics: 12th conference ASTM-STP-700; 1980. p. 189–221.